International Journal of Remote Sensing

ISSN: 0143-1161 (Print) 1366-5901 (Online) Journal homepage: www.tandfonline.com/journals/tres20

Benchmark studies on pixel-level spectral unmixing of multi-resolution hyperspectral imagery

C. V. S. S. Manohar Kumar, Sudhanshu Shekhar Jha, Rama Rao Nidamanuri & Vinay Kumar Dadhwal

To cite this article: C. V. S. S. Manohar Kumar, Sudhanshu Shekhar Jha, Rama Rao Nidamanuri & Vinay Kumar Dadhwal (2022) Benchmark studies on pixel-level spectral unmixing of multi-resolution hyperspectral imagery, International Journal of Remote Sensing, 43:4, 1451-1484, DOI: 10.1080/01431161.2022.2040755

To link to this article: https://doi.org/10.1080/01431161.2022.2040755

Published online: 09 Mar 2022.

INTERNATIONAL JOURNAL OF REMOTE SENSING
2022, VOL. 43, NO. 4, 1451–1484
https://doi.org/10.1080/01431161.2022.2040755

Taylor & Francis
Taylor & Francis Group

Benchmark studies on pixel-level spectral unmixing of multi-resolution hyperspectral imagery

C. V. S. S. Manohar Kumar[a], Sudhanshu Shekhar Jha[a], Rama Rao Nidamanuri[a] and Vinay Kumar Dadhwal[b]

[a]Department of Earth and Space Sciences, Indian Institute of Space Science and Technology, Department of Space, Government of India, Thiruvananthapuram, India; [b] National Institute of Advanced Studies, Bengaluru, India

ABSTRACT

Spectral unmixing-based estimation of material abundances in hyperspectral imagery has a variety of applications in mineralogy, environmental monitoring, agriculture, food processing, pharmacy, etc. A substantial body of literature is available on different inversion algorithms, optional pre-processing such as dimensionality reduction, and algorithms for endmembers extraction. The quality of abundance estimation depends on the number of materials, size, the geometrical orientation of materials, the source of endmembers, and the inversion algorithm used. However, there is a lack of studies on one-to-one assessment of the retrieval of abundances under various scenarios of spectral material distributions, the spatial resolution of the imagery, and the potential of in-situ reflectance measurements as candidate endmembers. The unavailability of comprehensive benchmark data coupled with pixel-to-pixel ground truth data has impeded comprehensive assessment of the first principles of spectral unmixing from a verifiable experimental perspective. The objective of this research is assessing the dynamics of material abundance as a function of the source of endmembers, spatial resolution, number of materials, and the size of materials. Linear and its sparse-based spectral unmixing algorithms were implemented on the datasets acquired for the estimation of abundances, considering the different scenarios of material distributions, spatial resolution, and the source of endmembers. We validated the results using pixel-to-pixel ground truth maps prepared for the different cases of spectral unmixing. The results provide answers to some critical open challenges in spectral unmixing, such as, (i) for an unambiguous detection, the fractional distribution of material has to be at least 1% of the pixel, (ii) endmembers from the in-situ spectra based on the external spectral library can offer reasonably good abundance estimates (an error of up to 20% compared to the image-based endmembers), and (iii) geometric orientations of materials in the ground sampling distance influence the abundance estimations. The benchmark dataset generated in this work is a valuable resource for addressing intriguing questions in spectral unmixing using hyperspectral imagery from a multi-resolution perspective.

ARTICLE HISTORY
Received 22 November 2021
Accepted 7 February 2022

KEY WORDS
Spectral Unmixing; Abundance Estimation; Hyperspectral Imagery; Material Mapping; Spectral Library; Endmembers

CONTACT C. V. S. S. Manohar Kumar rao@iist.ac.in Department of Earth and Space Sciences, Indian Institute of Space Science and Technology, Department of Space, Government of India, Valiamala, Thiruvananthapuram 695 547, India

1. Introduction

Spectral unmixing has been a method of choice for the detection and mapping of surface materials in coarse resolution remote sensing imagery. Several typical surface material compositions have been quantified at the sub-pixel level in a range of multispectral imagery (Keshava and Mustard 2002; Keshava 2003; Bioucas-Dias et al. 2012). However, due to the limited number of spectral bands and numerous different types of marginal surface distributions at the pixel level, sub-pixel material identification and mapping using spectral mixture modeling in multispectral imagery has met with limited success (Keshava 2003; Bullock, Woodcock and Olofsson 2020). Hyperspectral imagery has reinvigorated the prospects of spectral mixture modeling for sub-pixel material identification and mapping. Given the increasing sophistication of hyperspectral imaging sensors, there is a strong potential for general and targeted material identification and quantification at fractional pixel-scale using spectral mixture modeling (Adão et al. 2017; Hua et al. 2021). Operational application development for material identification and quantification in various domains such as mineral prospecting, precision agriculture, environmental monitoring with linear or intimate mixtures of materials is expected to be a realistic goal in the near future.

In the classical linear mixing model, there exists a linear relationship between the fractional abundance of the materials comprising the ground-sampling unit (pixel) and the spectral radiance recorded. If the total surface area is proportionally divided with spatial connectivity maintained conforming to the fractional distributions of the constituent materials, the linear unmixing of the pixel will yield the same proportions matching to the characteristics of the associated ground-sampling unit (Nascimento and Martín 2020; Li, Ma and Sidiropoulos 2021). Linear spectral unmixing has two consecutive steps: estimation of endmembers – the representative spectra of the constituent materials, and inversion – estimation of the associated fractional areal distributions of materials, generally called abundances, for each pixel. Typical to hyperspectral imagery, dimensionality reduction is an optional process for reducing data redundancy and managing computational load.

Endmember, a pure spectral signature equivalent of a material, is the distinct spectral response pattern spectrally exemplifying a material's physical and chemical properties (Nidamanuri and Zbell 2013). There are three approaches for acquiring endmembers for further application at the inversion stage of spectral unmixing. The first approach is the geometrical delineation of endmembers by mathematical extraction of extreme pixels projecting the respective hyperspectral imagery in a multidimensional feature space. Popular algorithms such as N-FINDR (Zortea and Plaza 2009; Park et al. 2021), pixel purity index (PPI) (Plaza and Chang 2005; Mishra, Govil and Srivastava 2021), vertex component analysis (VCA) (Nascimento and Dias 2005; Li, Ma and Sidiropoulos 2021), sequential maximum angle convex cone (SMACC) (Gruninger, Ratkowski and Hoke 2004; Cheng et al. 2021; Wei et al. 2021) belong to this approach. The second approach involves extensive human involvement wherein the endmembers are identified by human analyst delineation of select pixels from the locations known otherwise in the hyperspectral imagery. Endmember-candidate pixels identified using both the approaches are contextual. The endmembers are mathematically distinct but functionally indifferent, limiting the interpretation value in labeling and abundance quantification. Further, the endmembers

selected are highly analyst-dependable and are influenced by spectral and geometrical distortions, and noises. In the third approach, reference spectral library, the endmembers are collected from external sources, aggregating reference spectral measurements from reflectance measurement campaigns in-situ or under laboratory conditions (Cardoso-Fernandes et al. 2020; Hannula et al. 2020; Qi et al. 2020). Building upon the commercial availability of sophisticated spectroradiometers and the possible multi-dimensional application potential, there has been an upsurge in the developments of reflectance spectral libraries. For example, USGS spectral library (Hou et al. 2019; Zhang, Zhang and Jiao 2021), ECOSTRESS spectral library (Meerdink et al. 2019), and spectral library by CSIRO (Chabrillat et al. 2019; Janik, Soriano-Disla and Forrester 2020) are available for public usage. These libraries are populated with reference spectral measurements of thousands of material types collected over a period of time and space. The spectral libraries are expected to be useful for different applications such as target detection, classification, material prospecting, and identity verification. However, their potential for spectral unmixing of hyperspectral imagery is relatively unexplored.

During the last few years, several studies have attempted the unmixing of hyperspectral imagery, mainly focusing on the nature of inversion algorithms for unmixing under the linear versus non-linear mixing considerations (Li, Chen and Rahardja 2019; Borsoi, Imbiriba and Bermudez 2020a; Borsoi et al. 2020b; Drumetz, Chanussot and Jutten 2020; Hua et al. 2021; Qi et al. 2021). Some of the studies focus on algorithms imposing the spatial continuity (Ghasrodashti et al. 2017; Zhang et al. 2018a, 2018b; Feng, Wang and Zhong 2019; Palsson, Sveinsson and Ulfarsson 2019; Zhang et al. 2019; Cheng et al. 2021) and endmember variability (Uezato, Fauvel and Dobigeon 2018; Shah and Zaveri 2019; Xu, Du and Fan 2019) by simulation and using synthetic hyperspectral images. The estimated abundances from these algorithms are difficult to evaluate, and unconvincing procedures were used for the validation. The studies that used real hyperspectral images (Li et al. 2018; Palsson et al. 2018; Shi et al. 2018; Wang, Shi and Cui 2018; Zhang et al. 2018a; Heylen et al. 2019; Hong et al. 2019; Jin et al. 2019; Koirala et al. 2019; Feng and Fan 2021; Liu et al. 2021) have considered dominant land cover classes for abundance estimation. Consequently, the unmixing process has primarily been pursued from a land use/cover mapping perspective. Theoretically, spectral unmixing requires that the tangible abundance fraction of a mixed pixel be accounted for in the scene. Mathematics supports this theory when the spectral mixture-candidates are composed of areal fractions with a linear distribution. Given the possibility of several geometrical and radiometric distortions in the hyperspectral imagery, further compounded by the philosophical assumptions made about pixel-materials compositions, the smallest material fraction that can be retrieved is unknown. Understanding the vital issues of spectral unmixing requires hyperspectral images acquired with pixel-level knowledge-based ground-truth maps. Studies addressing these aspects of spectral unmixing are crucial for shedding light on theoretical considerations and practical implications (Zhao, Chen and He 2019; Cerra et al. 2021).

The number of materials vis-à-vis spatial resolution is considered the basis for attributing a pixel as pure or mixed. Considering the spatial resolution of the imagery as a fixed parameter, spectral unmixing has been used to estimate the endmembers and their abundances. However, the relationship between spectral reflectance and material abundance varies substantially across different spatial resolutions and governs the applicability

of the spectral unmixing results across various sensors. The spatial resolution influences the quality of endmembers retrieved from the imagery (Kizel and Benediktsson 2020). No studies have addressed the spectral unmixing problem from considering the same material's pure and mixed pixel spectra at different spatial resolutions. Reference datasets of multi-resolution hyperspectral imagery are vital for comprehensive studies on spectral unmixing.

To understand the practical application aspects of the spectral unmixing of hyperspectral imagery, equally applicable for multispectral imagery, and make pixel-level ground truth-linked hyperspectral imagery datasets available, we designed a multi-prong experimental set-up for hyperspectral imagery unmixing. The objectives of this paper are (i) to formulate a benchmark dataset for spectral mixture modeling of hyperspectral imagery and (ii) to perform quantitative analyses of the material-abundance estimations in hyperspectral imagery using linear spectral unmixing methods. Specifically, this paper attempts to answer the following questions of broader relevance to spectral unmixing.

(a) What is the functional accuracy of the estimated abundances in real hyperspectral imagery?
(b) What is the correlation between the abundances estimated using endmembers drawn from an independent spectral library and from the imagery itself?
(c) Considering linear spectral mixing, what is the smallest material abundance that can be unambiguously retrieved from a given spectral mixture?
(d) How does the number of endmembers in a mixed pixel affect the quality of abundance estimation?
(e) What is the impact of spatial resolution on the accuracy of abundance estimations?

To address these specific issues and advance the understanding of spectral mixing phenomena from the surface-material perspective (Figure 1), we acquired several hyperspectral datasets at different spatial resolutions under natural illumination using a ground-based terrestrial hyperspectral imager. Pixel level information on the composition of materials, endmembers and the different geometrical orientations and spatial distributions of materials were recorded. We present the details of the experimental set-up and the results of unmixing the acquired benchmark hyperspectral imagery from a semi-empirical evaluation of the proof-of-concept (PoC) perspective. Four algorithms belonging to two different categories were used for the identification and abundance estimations of various material candidates in the imagery. Results were validated by comparing with the ground truth maps generated for each scenario and using statistical measures.

2. Methodology

An overview of the methodology adopted is shown in Figure 2. Each element of the methodology: experimental design, methods used, generation of independent spectral libraries, various cases of spectral unmixing, and the validation method are described in the following sub-sections.

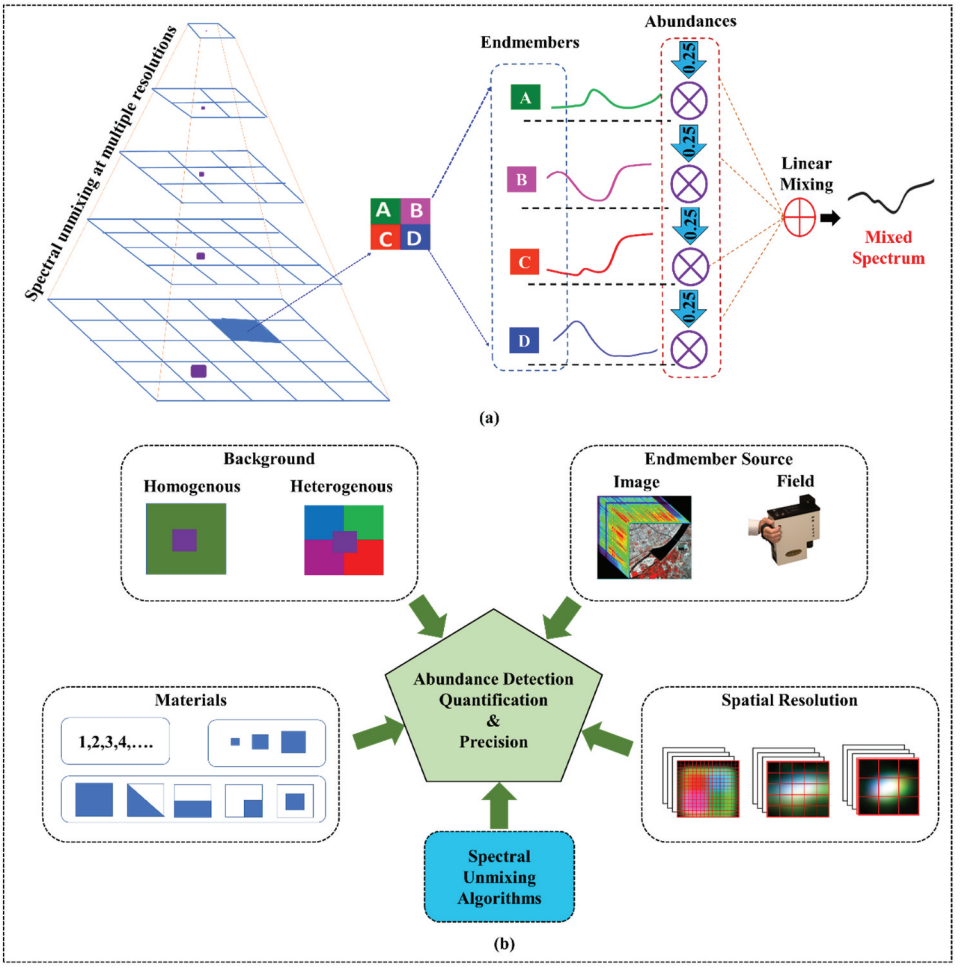

Figure 1. (a) Ideal case for linear spectral unmixing in a single pixel and the smallest fractional material in a pixel (represented by the violet color) across different spatial resolutions, and (b) impact of different factors on abundance estimation.

2.1. Experimental design and data acquisition

2.1.1. Spatial mixtures of materials and reference geometrical pixel positioning

At the functional level, spectral mixing of the radiance recorded by a remote sensor is the direct consequence of the presence and differential spatial distributions of various materials in the ground sampling distance (GSD), aka pixel. For an unambiguous realization of theoretical considerations in the spectral mixture modeling, the reference spectral data has to conform and meet key requirements – uniformity of texture, material types and hence their endmembers, known spatial dimensions of materials – areal fractions, nature of distribution in the GSD, and boundary adherence. Adhering to these key requirements, we conceptualize the reference data as an amalgamation of different color grids printed on a common printing material. Different types of colors represent different endmembers, and their spatial distribution apportions different types of materials. The boundaries of the printed color grids are

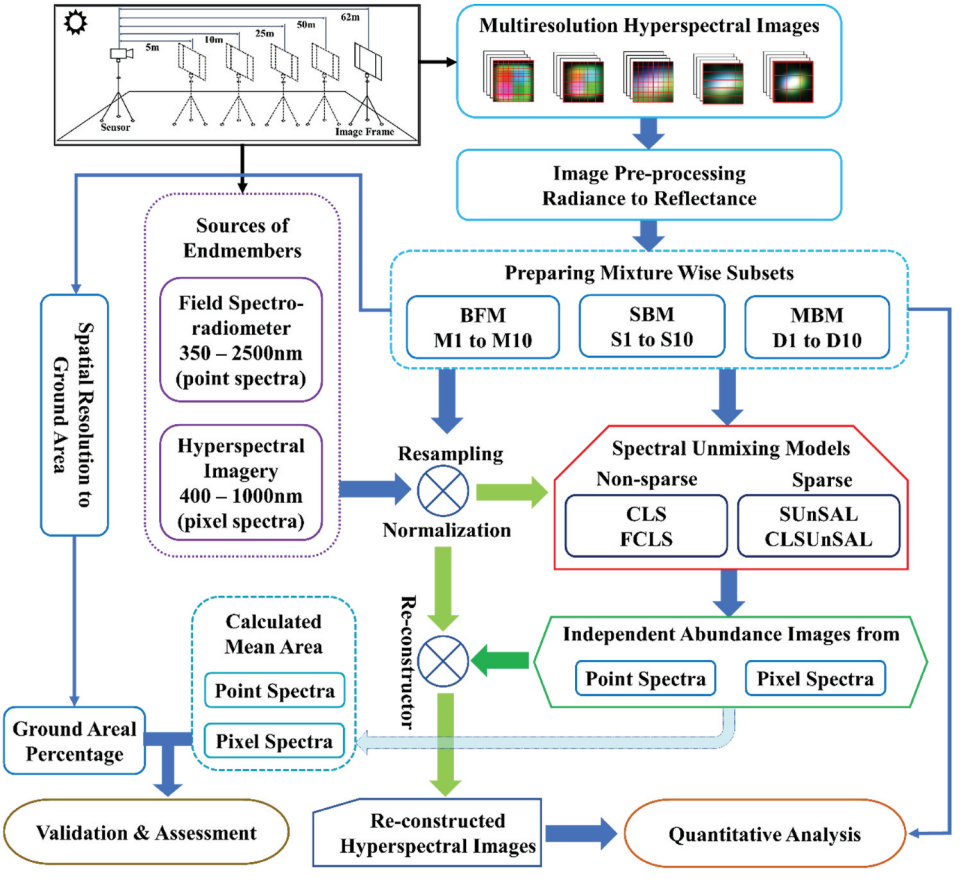

Figure 2. Overall methodological framework adopted for the study.

delineable. Different scenarios of the size, spatial distribution, and orientations of different materials can be realized by printing reference colors varying the area, spatial spread, and location in the print grid. Different cases of 'spectral mixtures' can be generated by forming different combinations of colors, sizes, orientations, and positioning. Analogous to imagery, each color grid represents a pixel. A single color grid represents a pure pixel; grids with different combinations of colors represent mixed pixels.

Satisfying the different data requirements of the objectives, we designed three different scenarios of spectral mixing, generating benchmark imagery with three different types of mixed pixels with five different spectral candidate colors – green, magenta, red, blue, and violent. Accordingly, there are three different datasets of imagery. The size of each color grid is 2 cm.

The first category of imagery contains pixels of pure colors without any local background. The dataset consists of five imagery of pure colors and five imagery of mixers of colors varied by size and spatial orientation. For ease of reference, we name this dataset as 'background-free-mixture (BFM)'. The detailed area proportions considered and the label assigned for each case of the spectral mixing are presented in Table 1, and the corresponding images are presented in RGB composition in Figure 3.

Table 1. Dataset-1: background-free mixture (BFM): areal proportions (%) and labeling of different cases of mixtures.

Mixture	Green	Magenta	Red	Blue	Violet
M1	100	0	0	0	0
M2	75	0	0	25	0
M3	50	0	25	25	0
M4	25	25	25	25	0
M5	0	0	50	50	0
M6	0	0	50	50	0
M7	0	100	0	0	0
M8	0	0	0	0	100
M9	0	0	100	0	0
M10	0	0	0	100	0

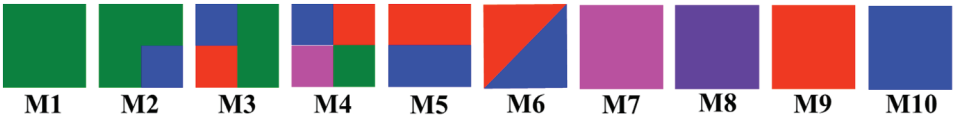

Figure 3. RGB representation of the different mixtures considered for dataset-1, background- free-mixture (BFM).

The second dataset contains ten imagery, with each imagery containing a different proportion of violet color on a green color local background. This is a mixture of two colors, foreground and background, representing two materials-endmembers. Named 'single-background-mixture (SBM)', the different areal proportions of the foreground considered, and its graphical representation are shown in Table 2 and Figure 4.

Table 2. Dataset-2: single background mixture (SBM): areal proportions (%) and labeling of different cases of mixtures.

	Background	Foreground
Mixture	Green	Violet
S1	99.75	0.25
S2	99	1
S3	97.75	2.25
S4	96	4
S5	93.75	6.25
S6	91	9
S7	87.75	12.25
S8	84	16
S9	79.75	20.25
S10	75	25

Figure 4. RGB composition of the different mixtures considered for dataset-2, single background mixture (SBM).

Table 3. Dataset-3: Areal proportions (%) and labeling of different cases of mixtures of multiple-background-mixture (MBM).

	Background				Foreground
Mixture	Green	Magenta	Red	Blue	Violet
D1	24.9375	24.9375	24.9375	24.9375	0.25
D2	24.75	24.75	24.75	24.75	1
D3	24.4375	24.4375	24.4375	24.4375	2.25
D4	24	24	24	24	4
D5	23.4375	23.4375	23.4375	23.4375	6.25
D6	22.75	22.75	22.75	22.75	9
D7	21.9375	21.9375	21.9375	21.9375	12.25
D8	21	21	21	21	16
D9	19.9375	19.9375	19.9375	19.9375	20.25
D10	18.75	18.75	18.75	18.75	25

The third case, named 'multiple-background-mixture (MBM)', is the combination of the first two cases – a single foreground color with different areal proportions portrayed on equal areal proportions of four different colors as local background. The different proportions considered, labeling and the graphical representation are presented in Table 3 and Figure 5.

There are ten different variations of the material-background distributions or orientations in each mixture scenario. The color grid materials were tightly affixed to a tripod-mounted wooden board coated in black. There was a radial distance of 10 cm between each pair of candidate mixture materials.

2.1.2. Imagery acquisition

The design of the proposed experimental set-up is shown in Figure 6. We used a terrestrial hyperspectral imager (THI) (Headwall Photonics, USA, A-series) to acquire hyperspectral imagery. The THI used is a high spectral resolution (854 spectral bands) pushbroom imaging system acquiring imagery in the 400 to 1000 nm region of the electromagnetic spectrum. The image size is determined by two system parameters: spatial pixels and object-space sampling interval. The THI has 1004 spatial pixels resulting in equivalent image size of 1004 rows. The object space sampling interval, yielding the number of columns, is controlled by the frame rate and the angular field of view and rotation speed of the rotating stage. The frame rate of the THI used is 90 and the rotating stage has 360° angular view with selectable rotational speed with 0.01 and 30^0 as minimum and maximum limits respectively. The rotational speed and number of spatial pixels can be optimized to suit the size of object-space being imaged. Imagery with different spatial resolutions can be acquired by altering the distance between the object-space and the

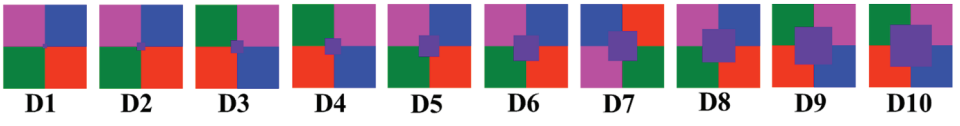

Figure 5. RGB representation of the different mixtures considered for dataset-2, multiple background mixture (MBM).

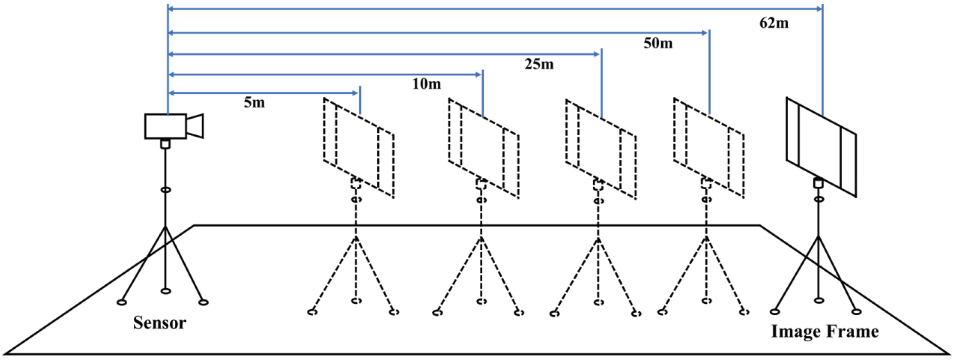

Figure 6. Synoptic view of the proposed experimental setup in sun light, acquired at different distances.

imaging system and using the objective lens of different focal lengths. Avoiding the problem of radiance signal saturation during the imagery acquisition process, the exposure time was manually adjusted. Exposure adjustment was done by focusing on a barium sulfate (white reference) until we observed a clear separation of the black and white lines on the camera live feed on the connected computer system. Based on the exposure time, the angular speed of the rotating stage was calculated and fed into the rotation stage control unit. We placed the white reference panel in the scene such that it lies within an area outside the targeted scene. We captured datasets of different spatial resolutions by maintaining different distances: 5 m, 10 m, 25 m, 50 m, and 62 m. The distance between the THI and the target scene was measured by a high accuracy laser distance meter.

2.1.3. Experimental data description

Corresponding to each mixture scenario, the candidate imagery representing the different variations of the materials' combination, background extent or orientation of the material distributions were extracted from the acquisition scene of the THÍ. In total, we acquired 30 candidate imagery potentially representing the different possibilities of spectral unmixing at the surface. To ensure all the foreground pixels' retention, the candidate imagery was extracted by allowing residual global background (black). The total number of foreground and background pixels in each candidate imagery was computed. Due to the practical limits of the imaging process and manual interventions, there is a marginal difference between the theoretical and actual number of target pixels. Details of the pixel composition of different candidate imagery at five different spatial resolutions for the ten different variations of the mixtures are presented in Table 4.

The THI acquires imagery in the radiance form. To enable data comparison across devices, and space-time scenarios, we calibrated and normalized the datasets to reflectance datacubes using the measurements acquired on the reference panel. Due to several external factors, and dynamic environmental conditions, the

Table 4. Number of target pixels in the candidate imagery at different spatial resolutions and material spatial proportions (fractions in the number of material pixels refer to the area excluded from a pixel due to boundary diffusion with background).

		Spatial resolution (cm)				
Area (%)	Area (cm^2)	0.16	0.32	0.80	1.61	1.99
		Number of foreground pixels				
100	4	154.565	38.641	6.183	1.546	1.005
75	3	115.924	28.981	4.637	1.159	0.754
50	2	77.283	19.321	3.091	0.773	0.503
25	1	38.641	9.660	1.546	0.386	0.251
0.25	0.01	0.386	0.097	0.015	0.004	0.003
1	0.04	1.546	0.386	0.062	0.015	0.010
2.25	0.09	3.478	0.869	0.139	0.035	0.023
4	0.16	6.183	1.546	0.247	0.062	0.040
6.25	0.25	9.660	2.415	0.386	0.097	0.063
9	0.36	13.911	3.478	0.556	0.139	0.090
12.25	0.49	18.934	4.734	0.757	0.189	0.123
16	0.64	24.730	6.183	0.989	0.247	0.161
20.25	0.81	31.299	7.825	1.252	0.313	0.204
25	1	38.641	9.660	1.546	0.386	0.251

reflectance datacubes exhibit local spikes or troughs in the spectral domain. We applied the Savitzky and Golay filter (Winkler 1993; Savitzky and Golay 1964), popularly known as the Savgol filter, for smoothing the datasets.

2.2. Reference spectral libraries – sources of endmembers

Apart from the methods of inversion, the source and quality of endmembers determine the nature of spectral unmixing and hence the validity of the abundances. Ensuring completeness and quality of material-spectrum, endmembers were extracted from two different sources – in-situ reflectance measurements and from the corresponding imagery for each case of the spectral unmixing considered. Concurrent with the time of imagery acquisition, the in-situ reflectance measurements were acquired using a full range (350 nm to 2500 nm) hyperspectral spectroradiometer (SVC, HR-1024i) with a spectral resolution of 3 nm in VNIR and 5 nm in SWIR, resulting in data acquisition in 1024 spectral bands. The distance between the spectroradiometer and the material object was optimized for acquiring measurements with an objective lens of a 4° field of view. Spectral measurements on a white reference panel coated with barium sulfate ($BaSO_4$) were also acquired for normalization and further computation of the reflectance spectra of the candidate materials. Each spectrum was measured by taking an average of ten intermediate spectral samples.

The THI acquires imagery in the VNIR range, 400–1000 nm. To make the spectral comparisons meaningful between the two different sources of endmember spectra, the in-situ spectral measurements were resampled to the spectral coverage and bandwidth of the THI. The spectral reflectance measurements were further organized in the form of spectral libraries with the flexibility of changing entries to reflect the experimental conditions of spectral unmixing in each spectral unmixing scenario. Figure 7 shows the mean spectral profiles of the color-material candidates considered from the spectroradiometer and the THI.

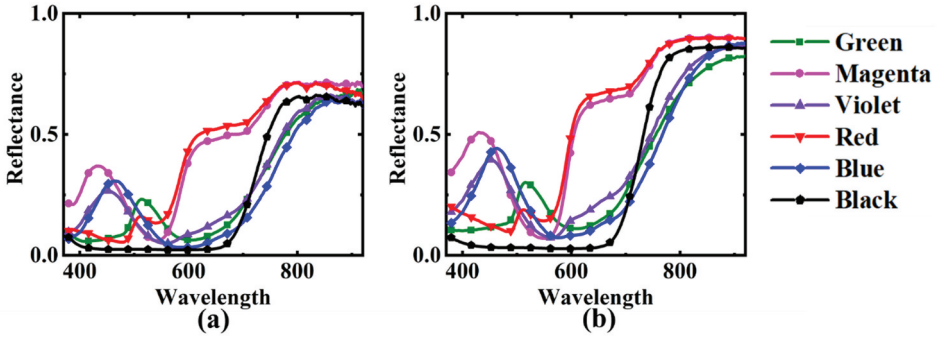

Figure 7. Spectral profiles of the candidate color-materials acquired from (a) terrestrial hyperspectral imager, and (b) from in-situ spectral measurements (external spectral library).

2.3. Spectral unmixing models

The benchmark datasets acquired are suitable for studying the linear and non-linear spectral unmixing categories from a range of spectral mixture modeling perspectives. Within the purview of this work, we considered experimental implementation from the linear spectral unmixing (LSU) perspective. Further, we implemented sparsity-based spectral unmixing algorithms to assess the applicability of endmembers extracted from the in-situ spectral library. Since the aim is not the development of new spectral unmixing algorithms per se, we considered two recent linear spectral unmixing algorithms with further development to the sparse unmixing method. We present a brief description of the algorithms used. Readers may refer to the citation for a detailed mathematical treatment of the algorithms.

In the LSU, the signal received at the sensor $y_i, (i \in \{1, 2, 3, \ldots .n\})$ in n-bands is represented as:

$$y_i = \sum_{m=1}^{m} a_m e_{i,m} + \eta_i \tag{1}$$

where, $e_{\mathbf{i,m}}$ is the m^{th} endmember at a i^{th}- band, a_m is the amount of the fractional abundance of the m^{th} endmember and η_i is noise caused due to the scattering effects in the path between the ground to the sensor in addition to the internal noise of the sensor (Eismann 2012).

Extending Equation (1) to a hyperspectral data matrix $Y = \left[y_1, y_2, \ldots .y_p\right]$, we rewrite it as:

$$Y = AE + \eta \tag{2}$$

where $A = \left[a_1, a_2, \ldots .a_p\right]$ is the abundance matrix, and $\eta = \left[\eta_1, \eta_2, \ldots .\eta_{\mathbf{p}}\right]$ is the noise matrix.

Mathematically, LSU is a constraint problem where the abundance must be either positive or zero, i.e. $(a \geq 0)$ (known as abundance non-negativity constraint (ANC)). Further, the sum of all abundances must be equal to one, i.e. $\left(1^T a = 1\right)$(known as

abundance sum constraint (ASC)). These constraints give rise to two categories of problems, popularly known as constraint least square (CLS) problem and fully constraint least square (FCLS) (Bioucas-Dias and Figueiredo 2010) problem, represented as:

$$\mathrm{CLS} = > (\mathrm{P_{CLS}}) : \min_{a} \frac{1}{2} \|\mathbf{AE} - \mathbf{Y}\|_2^2 \text{Subject to } a \geq 0 \tag{3}$$

$$\mathrm{FCLS} = > (\mathrm{P_{FCLS}}) : \min_{\mathrm{a}} \frac{1}{2} \|\mathbf{AE} - \mathbf{Y}\|_2^2 \text{Subject to a} \geq 0, 1^{\mathrm{T}}\mathrm{a} = 1. \tag{4}$$

The sparsity-based spectral unmixing can be obtained by transforming Equation (3) to a sparse regression problem (Bioucas-Dias and Figueiredo 2010; Iordache, Bioucas-Dias and Plaza 2011) and solving through the alternating direction method of multipliers (ADMM) (Bioucas-Dias 2009). For ease of reference, we name this algorithm as SUnSAL (spectral unmixing by splitting and augmented Lagrangian) and express it as:

$$\mathrm{SUnSAL} = > \left(\mathrm{P_{Sparse}}\right) : \min_{a} \frac{1}{2} \| AE - Y \|_2^2 + \lambda \| a\|_1 + I_{R_+^n}(E) \tag{5}$$

$$subjectgttogta \geq 0$$

where $\|.\|_2$ and $\|.\|_1$ are ℓ_2 and ℓ_1 norms respectively; λ is a controlling parameter between two norms; $I_{R_+^n}(E) = \sum_{i=1}^{n} I_{R_+^n}(e_i)$ is an indicator function related to the spectral library. Equating $\lambda = 0$ in Equation (5), SUnSAL reduces to CLS problem.

The second unmixing algorithm, Collaborative Sparse Unmixing via variable Splitting and Augmented Lagrangian (CLSUnSAL), is an FCLS variant of the SUnSAL algorithm (Iordache, Bioucas-Dias and Plaza 2014) expressed in Equation (6).

$$\mathrm{CLSUnSAL} = < \left(\mathrm{P}_{CollaborativeSparse}\right) : \min_{\mathrm{a}} \| \mathbf{AE} - \mathbf{Y} \|_{\mathrm{F}}^2 + \lambda \sum_{\mathrm{k}=1}^{\mathrm{m}} \| \mathbf{a^k}\|_{2,1} + \mathrm{I}_{\{1\}}\left(1^{\mathrm{T}}\mathbf{E}\right) + \mathrm{I}_{\mathrm{R}_+^{\mathrm{n}}}(\mathbf{E}) \tag{6}$$

$$subjectgttogt\mathbf{a} \geq 0, 1^{\mathbf{T}}\mathbf{a} = 1.$$

In Equation (6), $\sum_{k=1}^{m} \| \mathrm{a}^{\mathrm{k}}\|_{2,1}$ is $\ell_{2,1}$ mixed norm that provides the sparse solution and, X_F is the Frobenius norm, and $\lambda > 0$ is the regularization parameter.

2.4. Validation and quantitative analysis

The performance of the spectral unmixing results for the various cases are validated at two levels- overall imagery and pixel-level using two widely used statistical measures.

At the pixel level, the quality of spectral unmixing has been assessed using the pixel-wise root mean square error (S – RMSE) computed between the input hyperspectral imagery (Y) and the reconstructed hyperspectral image ($\widehat{Y}$) and is given by:

$$S - RMSE = \sqrt{\frac{\sum_{i=1}^{n} \left(y_{p_i} - \widehat{y_{p_i}}\right)^2}{n}}. \tag{7}$$

For the functional area comparison, the quality of estimated abundance has been assessed using the relative areal error computed between ground truth area (a) and calculated mean abundance area ($\hat{a}$) for each material and is given by:

$$Relativearealerror = \frac{\hat{a} - a}{a} \times 100. \tag{8}$$

3. Results and analysis

We present the results of the material abundances estimated from the imagery datasets as a function of background, number of materials, source of endmembers, inversion algorithms, and spatial resolution detailing the nature of matching and the error of estimation. For ease of readability, we organize the experimental results into different cases.

3.1. Case-1: When there are different numbers of materials in each pixel and are without local background

When there was only one material in the pixel and its endmember was extracted from the imagery, the estimated abundance matches ground truth-value across the algorithms with 99.9% accuracy (see Table 5). The apparent residual values of the relative areal error (Table 6) confirm the closeness of the estimated and the actual abundances. However, if the source of endmember was the external spectral library, the best retrieval percentage of the abundances dropped to about 81%. Similar to the pattern observed with the image-based endmember, the abundance retrievals from the external spectral library are consistent across the algorithms. However, the magnitude of the abundance changed substantially by the material type for both the sources of endmembers. The estimated abundances are stable across the spatial resolutions for the endmember extracted from the imagery. However, the abundances estimated from using the external spectral library as the endmember source indicate two distinct patterns of variation. First, the overall magnitude of the abundance estimated is about 20% lesser than the abundance estimated from the image-based endmember (see Figure 8). Second, the within-material abundance variation is relatively lesser even if the spatial resolution changes. The observed abundance trend is also reflected in the error estimates as quantified by S-RMSE (Figure 9).

When there are three materials in each pixel, the best estimate of abundance is 88% and 77%, respectively, for the endmembers extracted from the imagery and the external spectral library (Figure 10 and Table 7). The best material-specific distributions of the abundance are 24.86%, 24.85% and 38.54%, respectively, for the imagery with mixtures of 25%, 25% and 50%. If the endmembers are extracted from the external spectral library, the best abundance distributions are 18.42%, 25.42%, and 33.24%. The intra-material variation of the abundances for the material with a smaller fraction is marginal across the spatial resolutions and sources of endmembers. However, the material with a large fraction (50%) exhibits substantial underestimation compared to the materials of smaller fractions. The trend is the same across the inversion algorithms and the source of endmembers.

Table 5. Summary of the material abundances estimated (in %) when there is only one material in the hyperspectral imagery and without local background (endmembers: Image – from the imagery; Field – from the external spectral library).

		Spatial Resolution (cm)									
		0.16		0.32		0.8		1.61		1.99	
		Endmember source									
Mixture (Material) (Actual %)	Algorithm	Image	Field	Image	Field	Image	Field	Image	Field	Image	Field
M1 (Green) (100)	CLS	99.93	81.71	97.73	81.25	92.26	81.66	73.21	73.63	66.10	69.68
	SUnSAL	99.92	81.71	97.72	81.25	92.25	81.69	73.20	73.65	66.08	69.65
	FCLS	99.87	78.54	97.09	78.99	90.13	78.44	68.95	69.71	63.43	69.88
	CLSUnSAL	99.87	78.54	97.09	78.99	90.13	78.43	68.95	69.78	63.44	69.91
M7 (Magenta) (100)	CLS	86.66	68.75	88.69	70.58	88.49	70.69	82.97	67.25	79.72	64.78
	SUnSAL	86.66	68.75	88.70	70.58	88.51	70.71	83.01	67.29	79.76	64.81
	FCLS	86.42	67.27	89.60	69.50	93.82	69.47	92.74	67.35	87.25	63.08
	CLSUnSAL	86.42	67.27	89.60	69.50	93.82	69.47	92.74	67.35	87.25	63.08
M8 (Violet) (100)	CLS	82.71	63.09	86.71	65.34	86.23	60.90	95.72	58.06	93.57	54.01
	SUnSAL	82.71	63.09	86.71	65.35	86.23	60.90	95.72	58.07	93.57	54.03
	FCLS	82.81	60.19	86.67	64.20	85.86	59.29	95.26	55.41	92.99	50.13
	CLSUnSAL	82.81	60.19	86.67	64.20	85.86	59.29	95.26	55.41	92.99	50.14
M9 (Red) (100)	CLS	93.03	78.94	92.77	79.58	89.99	82.30	85.69	83.38	75.00	74.46
	SUnSAL	93.03	78.94	92.77	79.58	90.01	82.32	85.72	83.41	75.03	74.49
	FCLS	92.58	77.13	92.82	77.91	92.50	77.11	94.02	80.01	81.79	70.98
	CLSUnSAL	92.58	77.13	92.82	77.91	92.50	77.11	94.02	80.01	81.79	70.98
M10 (Blue) (100)	CLS	90.08	68.52	91.15	69.36	88.46	65.39	92.27	59.37	89.17	55.88
	SUnSAL	90.08	68.52	91.14	69.36	88.44	65.38	92.22	59.36	89.12	55.86
	FCLS	89.98	66.07	90.59	66.96	85.21	64.98	83.13	58.93	83.32	57.37
	CLSUnSAL	89.98	66.07	90.59	66.96	85.21	64.98	83.13	58.95	83.32	57.40

Table 6. Summary of the relative areal error (%) in the abundances estimated when there is only one material in the hyperspectral imagery and is without local background (endmembers: Image – from the imagery; Field – from the external spectral library).

		Spatial Resolution (cm)									
		0.16		0.32		0.8		1.61		1.99	
		Endmember source									
Mixture (Material)	Algorithm	Image	Field	Image	Field	Image	Field	Image	Field	Image	Field
M1 (Green)	CLS	−0.07	−18.29	−2.27	−18.75	−7.74	−18.34	−26.79	−26.37	−33.90	−30.32
	SUnSAL	−0.08	−18.29	−2.28	−18.75	−7.75	−18.31	−26.80	−26.35	−33.92	−30.35
	FCLS	−0.13	−21.46	−2.91	−21.01	−9.87	−21.56	−31.05	−30.29	−36.57	−30.12
	CLSUnSAL	−0.13	−21.46	−2.91	−21.01	−9.87	−21.57	−31.05	−30.22	−36.56	−30.09
M7 (Magenta)	CLS	−13.34	−31.25	−11.31	−29.42	−11.51	−29.31	−17.03	−32.75	−20.28	−35.22
	SUnSAL	−13.34	−31.25	−11.30	−29.42	−11.49	−29.29	−16.99	−32.71	−20.24	−35.19
	FCLS	−13.58	−32.73	−10.40	−30.50	−6.18	−30.53	−7.26	−32.65	−12.75	−36.92
	CLSUnSAL	−13.58	−32.73	−10.40	−30.50	−6.18	−30.53	−7.26	−32.65	−12.75	−36.92
M8 (Violet)	CLS	−17.29	−36.91	−13.29	−34.66	−13.77	−39.10	−4.28	−41.94	−6.43	−45.99
	SUnSAL	−17.29	−36.91	−13.29	−34.65	−13.77	−39.10	−4.28	−41.93	−6.43	−45.97
	FCLS	−17.19	−39.81	−13.33	−35.80	−14.14	−40.71	−4.74	−44.59	−7.01	−49.87
	CLSUnSAL	−17.19	−39.81	−13.33	−35.80	−14.14	−40.71	−4.74	−44.59	−7.01	−49.86
M9 (Red)	CLS	−6.97	−21.06	−7.23	−20.42	−10.01	−17.70	−14.31	−16.62	−25.00	−25.54
	SUnSAL	−6.97	−21.06	−7.23	−20.42	−9.99	−17.68	−14.28	−16.59	−24.97	−25.51
	FCLS	−7.42	−22.87	−7.18	−22.09	−7.50	−22.89	−5.98	−19.99	−18.21	−29.02
	CLSUnSAL	−7.42	−22.87	−7.18	−22.09	−7.50	−22.89	−5.98	−19.99	−18.21	−29.02
M10 (Blue)	CLS	−9.92	−31.48	−8.85	−30.64	−11.54	−34.61	−7.73	−40.63	−10.83	−44.12
	SUnSAL	−9.92	−31.48	−8.86	−30.64	−11.56	−34.62	−7.78	−40.64	−10.88	−44.14
	FCLS	−10.02	−33.93	−9.41	−33.04	−14.79	−35.02	−16.87	−41.07	−16.68	−42.63
	CLSUnSAL	−10.02	−33.93	−9.41	−33.04	−14.79	−35.02	−16.87	−41.05	−16.68	−42.60

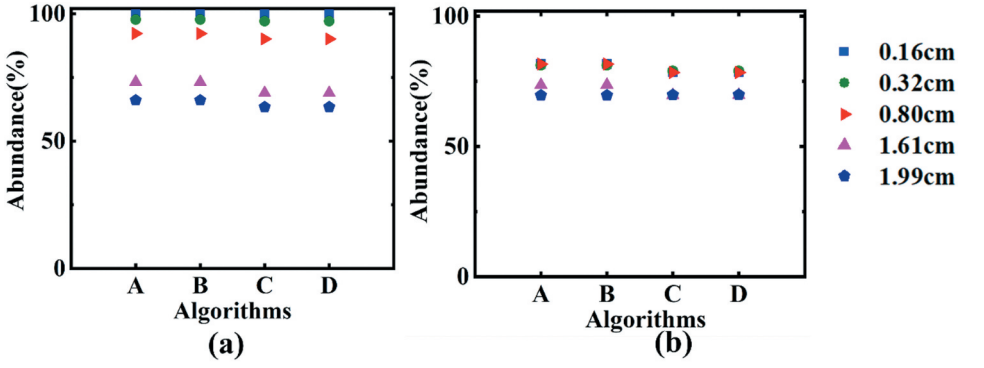

Figure 8. Estimated abundances and corresponding S – RMSE from different inversion algorithms at different spatial resolutions ((a) 0.16 cm, (b) 0.32 cm, (c) 0.80 cm, (d) 1.61 cm, and (e) 1.99 cm) when there is only one material with no local background using imagery (I) and external spectral library (F) endmember source for green (M1), magenta (M7), violet (M8), red (M9), and blue (M10) materials.

The material abundances estimated from the hyperspectral imagery containing four different materials of equal size (25% each) are shown in Figure 11 and Table 8. When the source of endmembers is the imagery, the best estimate of abundance is about 108%, with 25.99%, 25.08%, 29.71% and 28.13% being the respective abundances for the four different materials. There is a moderate underestimation in the best estimate of abundance, (total 94.61%), with 23.21%, 24.58%, 25.32%, and 21.50% being the individual fractions of the materials when the endmembers were extracted from the external spectral library. However, the abundance estimates are greatly varied by the spatial resolution and material type, as evident from Figure 8 Compared to the results obtained from the imagery retrieved endmembers, the results obtained from the external library-derived endmembers are stable in that there is an underestimation by 14% to 60% consistent across the spatial resolution. Continuing the patterns observed in the previous cases, the influence of inversion algorithms on the abundances is marginal.

3.2. Case-2: Two materials in each pixel of the hyperspectral imagery and the effect of the difference in material's fractional size

Material abundances estimated from the hyperspectral imagery, when each pixel was composed of only two materials are presented in Figure 12 and Table 9. Results are presented for two different spatial orientations of the materials in the imagery. When the source of endmember was the imagery, the best estimate of abundance for the two different material types is 49.5%, a close match with the ground truth (50%). When the source of the endmember was the external spectral library, the most probable abundance is 40%. However, the abundance reduced substantially at coarser spatial resolutions and varied across the material types. When the spatial orientation of the two material segments is changed, there is a marginal difference of about 2% compared to the best case of estimation.

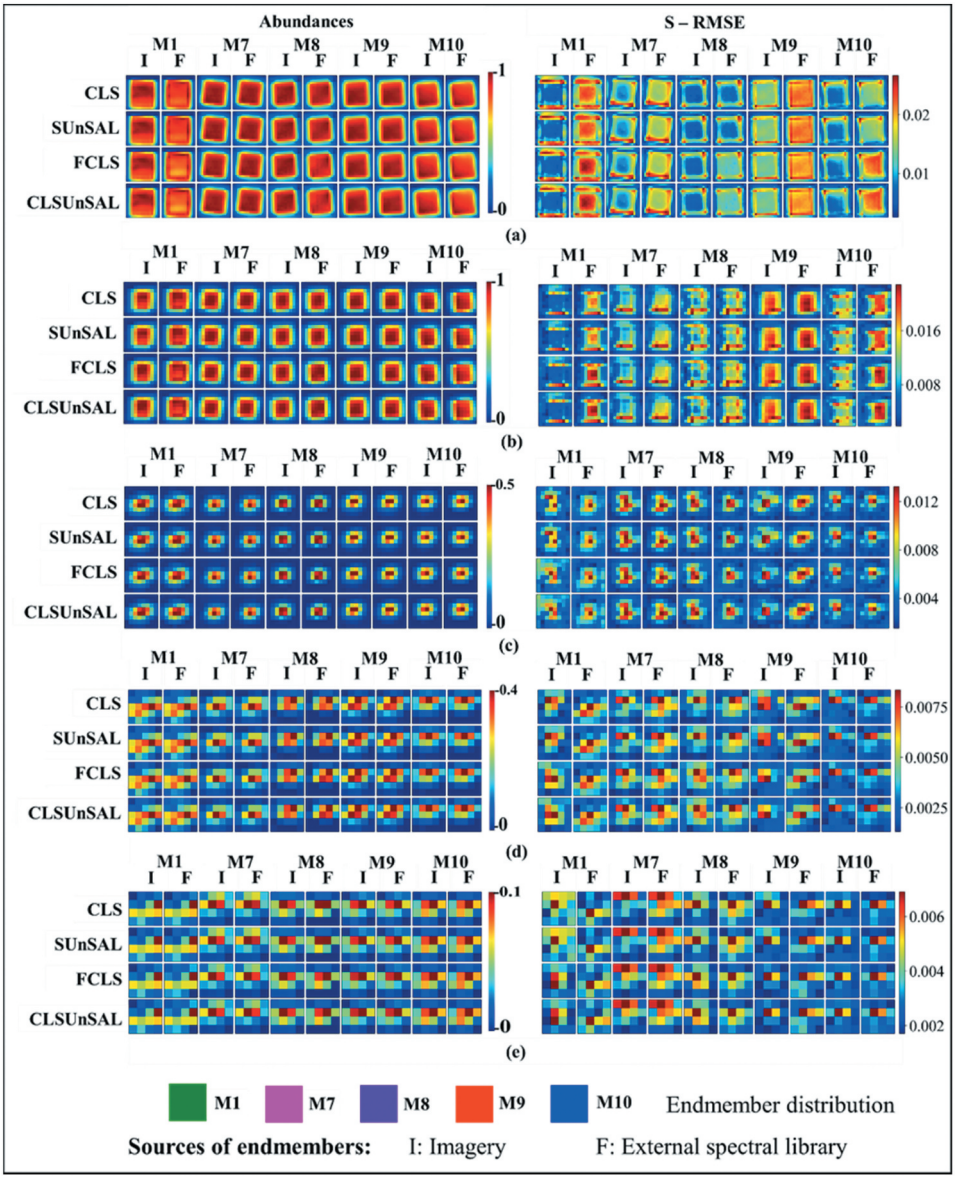

Figure 9. Variation of the estimated abundances as a function of spatial resolution for the green material (M1) for different algorithms CLS (A), SUnSAL (B), FCLS (C), and CLSUnSAL (D) for endmember extracted from (a) imagery, and (b) external spectral library.

Materials of different sizes: When the hyperspectral imagery contained only two materials with areal extents 75% and 25%, respectively, the abundances estimated exhibit contrasting patterns (Figure 13 and Table 10). The best estimates of abundances from the imagery-based endmembers match very closely (74.15% and 23.54%) with the ground reference abundance values. When the source of endmembers is the external spectral library, the best estimates of abundances are 66.23% and 17.93%, significant under-estimation (9%) compared to the reference abundance values. The response of

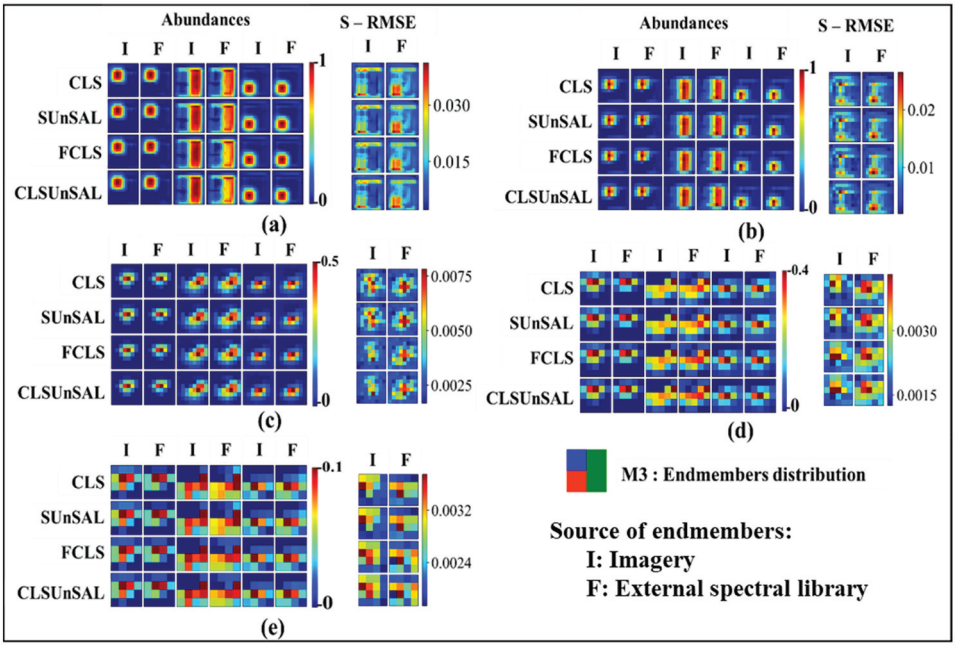

Figure 10. For different spatial resolutions ((a) 0.16 cm, (b) 0.32 cm, (c) 0.80 cm, (d) 1.61 cm, and (e) 1.99 cm) abundance estimates with error score (S-RMSE) when the hyperspectral imagery contained three different materials with no local background influence.

abundance estimates to the changing spatial resolution presents two distinct patterns. The estimated abundances decrease as the spatial resolution becomes coarser. However, the rate of decrease is material-type dependent, as indicated by the size of the material candidate. The highest decrease of about 40% is observed for the material with 75% reference abundance endmembers. The range of difference in the abundances estimated

Table 7. Summary of the material abundances estimated when there are only three materials in the hyperspectral imagery and without local background (endmembers: Image – from the imagery; Field – from the external spectral library).

		Spatial Resolution (cm)									
		0.16		0.32		0.8		1.61		1.99	
		Endmember source									
Mixture Material Actual %	Algorithm	Image	Field	Image	Field	Image	Field	Image	Field	Image	Field
M3 (Blue) (25%)	CLS	22.44	16.80	24.86	18.42	25.42	17.32	30.73	17.06	31.63	17.43
	SUnSAL	22.44	16.80	24.86	18.42	25.42	17.32	30.72	17.06	31.62	17.43
	FCLS	22.38	16.63	24.19	18.16	25.17	17.27	30.13	17.77	30.74	17.79
	CLSUnSAL	22.38	16.63	24.19	18.16	25.17	17.27	30.12	17.77	30.74	17.79
M3 (Green) (50%)	CLS	38.22	32.13	36.92	33.24	32.66	32.33	23.11	26.60	17.55	24.19
	SUnSAL	38.22	32.13	36.92	33.24	32.66	32.34	23.12	26.63	17.55	24.20
	FCLS	38.54	32.23	36.45	33.01	33.02	30.16	24.31	23.95	18.25	21.61
	CLSUnSAL	38.54	32.23	36.45	33.01	33.02	30.16	24.31	23.95	18.24	21.62
M3 (Red) (25%)	CLS	23.89	20.32	25.80	22.53	24.83	25.50	24.56	27.96	20.34	24.24
	SUnSAL	23.90	20.33	25.80	22.54	24.85	25.52	24.59	27.99	20.37	24.26
	FCLS	23.83	19.40	26.05	21.48	28.25	21.98	31.95	25.42	25.27	20.95
	CLSUnSAL	23.83	19.40	26.05	21.48	28.24	21.97	31.95	25.42	25.26	20.95

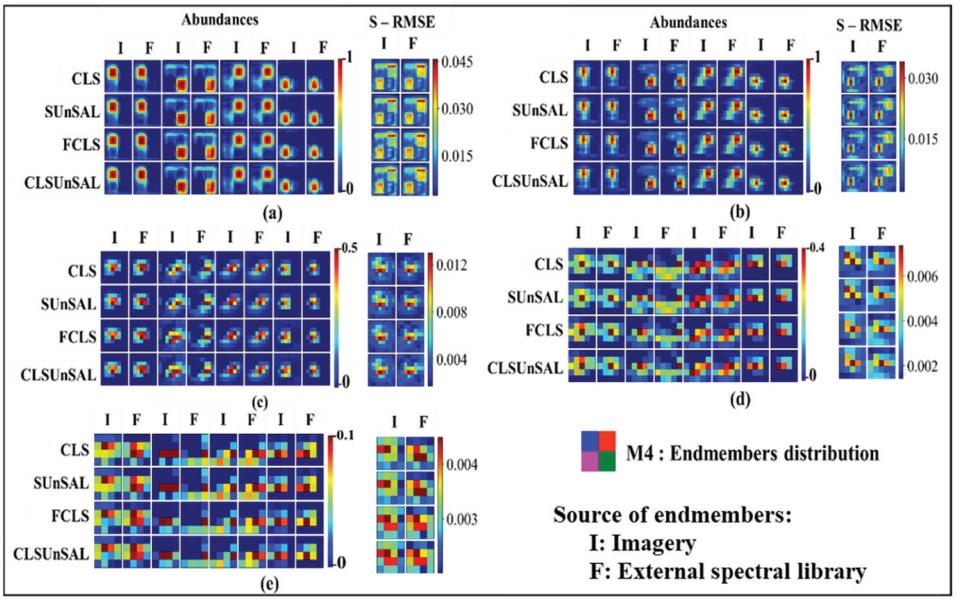

Figure 11. Quantitative comparison of the abundances estimated and the corresponding S-RMSE at different spatial resolutions (a) 0.16 cm, (b) 0.32 cm, (c) 0.80 cm, (d) 1.61 cm, and (e) 1.99 cm through different unmixing algorithms.

at different resolutions is about 5% for both the imagery and external spectral library-based endmembers. The impact of spatial resolution on the abundances is very high on the imagery-based endmembers compared to the external spectral library.

Table 8. Summary of the material abundances estimated when there are only four materials in the hyperspectral imagery and without local background (endmembers: Image – from the imagery; Field – from the external spectral library).

		Spatial Resolution (cm)									
		0.16		0.32		0.8		1.61		1.99	
		Endmember source									
Mixture Material Actual %	Algorithm	Image	Field	Image	Field	Image	Field	Image	Field	Image	Field
M4 (Blue) (25%)	CLS	27.69	19.59	32.10	22.47	29.23	20.27	38.49	23.08	34.76	20.22
	SUnSAL	27.69	19.59	32.09	22.47	29.22	20.26	38.47	23.08	34.73	20.21
	FCLS	25.99	20.96	29.75	23.21	26.05	20.05	31.15	22.43	28.53	20.96
	CLSUnSAL	25.99	20.96	29.75	23.21	26.04	20.05	31.15	22.43	28.54	20.96
M4 (Green) (25%)	CLS	31.71	27.89	25.26	24.03	19.07	17.29	11.88	18.43	8.82	12.29
	SUnSAL	31.70	27.89	25.26	24.03	19.08	17.30	11.91	18.45	8.84	12.30
	FCLS	32.56	29.38	25.68	24.58	27.31	15.85	25.09	14.94	18.78	9.95
	CLSUnSAL	32.56	29.38	25.68	24.58	27.31	15.85	25.08	14.94	18.75	9.98
M4 (Red) (25%)	CLS	33.30	28.56	34.87	30.32	31.26	33.20	30.75	35.34	19.89	25.32
	SUnSAL	33.30	28.56	34.87	30.32	31.26	33.21	30.76	35.36	19.90	25.33
	FCLS	32.34	28.93	33.89	30.13	30.80	29.77	29.71	31.32	18.01	22.99
	CLSUnSAL	32.34	28.93	33.89	30.13	30.80	29.76	29.72	31.32	18.02	22.99
M4 (Magenta) (25%)	CLS	14.18	10.43	13.86	10.23	15.16	8.26	18.25	11.19	21.47	13.06
	SUnSAL	14.18	10.43	13.86	10.23	15.17	8.27	18.27	11.20	21.50	13.07
	FCLS	15.24	9.55	15.08	9.56	20.93	8.45	28.13	11.58	28.94	11.23
	CLSUnSAL	15.24	9.55	15.08	9.56	20.93	8.44	28.13	11.57	28.92	11.23

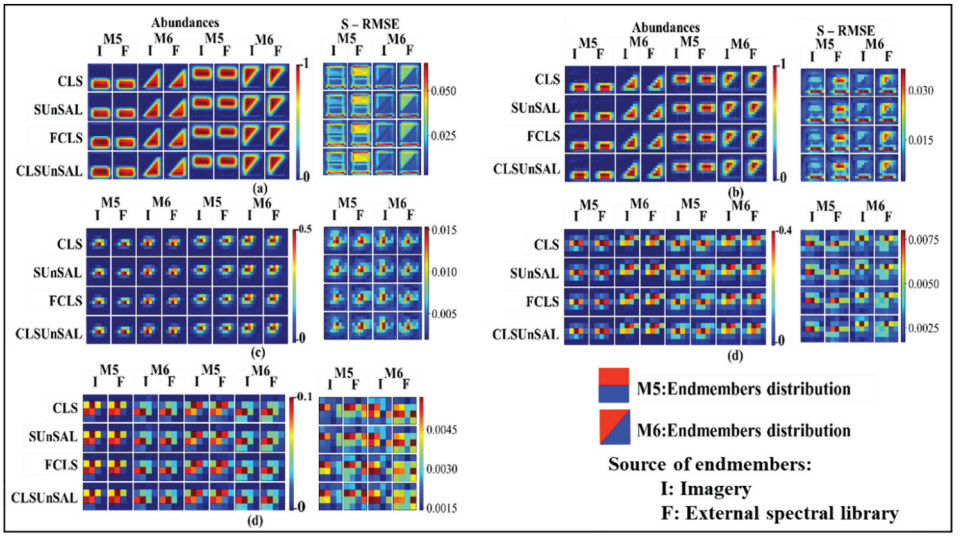

Figure 12. Estimated abundances and the corresponding S – RMSE from different inversion algorithms at different spatial resolutions ((a) 0.16 cm, (b) 0.32 cm, (c) 0.80 cm, (d) 1.61 cm, and (e) 1.99 cm) when there are only two materials with no local background in the hyperspectral imagery.

3.3. Case-3: When the pixel in the hyperspectral imagery has homogenous background and has only one material of different fractions

Abundance estimations for the case of hyperspectral imagery with a homogenous background and with different discrete fractions of a single material (ranging from 0.25% to 25%) are summarized in Table 11 and Figure 14. When the material occupies only 0.25% in

Table 9. Summary of the material abundances estimated when there are only two materials in the hyperspectral imagery and are without local background (endmembers: Image – from the imagery; Field – from the external spectral library).

		Spatial Resolution (cm)									
		0.16		0.32		0.8		1.61		1.99	
		Endmember source									
Mixture Material Actual %	Algorithm	Image	Field	Image	Field	Image	Field	Image	Field	Image	Field
M5 (Blue) (50%)	CLS	48.63	37.43	46.46	35.45	46.84	31.06	51.99	31.35	41.93	24.68
	SUnSAL	48.63	37.43	46.46	35.45	46.84	31.06	51.99	31.36	41.93	24.69
	FCLS	46.50	37.89	44.82	35.54	47.23	30.97	54.23	32.15	42.96	24.62
	CLSUnSAL	46.50	37.89	44.82	35.54	47.23	30.97	54.23	32.15	42.95	24.62
M5 (Red) (50%)	CLS	43.09	36.21	42.37	36.04	42.48	38.99	39.82	39.90	34.54	35.29
	SUnSAL	43.09	36.21	42.37	36.05	42.49	39.01	39.85	39.93	34.57	35.31
	FCLS	42.74	35.46	42.67	35.26	46.82	36.40	49.05	39.06	40.62	32.56
	CLSUnSAL	42.74	35.46	42.67	35.26	46.82	36.40	49.05	39.06	40.62	32.56
M6 (Blue) (50%)	CLS	43.68	32.83	45.51	33.56	43.95	28.30	48.26	29.38	50.04	29.10
	SUnSAL	43.68	32.83	45.51	33.56	43.95	28.30	48.27	29.38	50.04	29.11
	FCLS	43.19	32.92	44.73	33.47	44.16	28.15	49.19	29.33	49.72	29.00
	CLSUnSAL	43.19	32.92	44.73	33.47	44.15	28.14	49.19	29.33	49.72	29.00
M6 (Red) (50%)	CLS	45.05	37.55	46.10	38.70	44.25	40.27	41.29	41.79	34.72	34.19
	SUnSAL	45.05	37.55	46.11	38.70	44.27	40.30	41.32	41.82	34.74	34.22
	FCLS	44.39	36.38	46.16	37.53	47.29	36.48	48.00	38.21	39.48	30.87
	CLSUnSAL	44.39	36.38	46.16	37.53	47.29	36.48	48.00	38.21	39.48	30.87

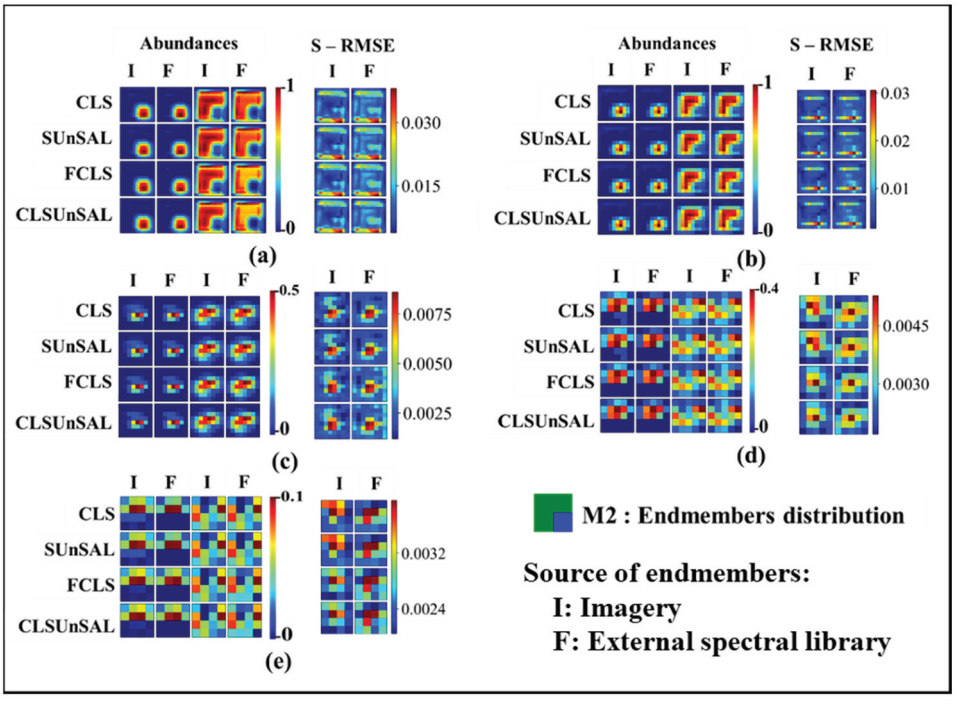

Figure 13. Estimates of abundances and the corresponding S – RMSE for the case of spectral unmixing of hyperspectral imagery of different spatial resolutions ((a) 0.16 cm, (b) 0.32 cm, (c) 0.80 cm, (d) 1.61 cm, and (e) 1.99 cm) and form different inversion algorithms.

Table 10. Summary of the material abundances estimated when there are only two materials in the hyperspectral imagery and without local background (endmembers: Image – from the imagery; Field – from the external spectral library).

		Spatial Resolution (cm)									
		0.16		0.32		0.8		1.61		1.99	
		Endmember source									
Mixture Material Actual %	Algorithm	Image	Field	Image	Field	Image	Field	Image	Field	Image	Field
M2 (Blue) (25%)	CLS	22.08	16.87	23.54	17.82	21.99	15.07	26.95	13.10	27.84	12.90
	SUnSAL	22.08	16.87	23.54	17.82	21.98	15.06	26.91	13.09	27.80	12.89
	FCLS	21.95	16.84	22.49	17.93	19.06	15.01	20.12	13.41	21.95	14.49
	CLSUnSAL	21.95	16.84	22.49	17.93	19.06	15.01	20.12	13.41	21.95	14.49
M2 (Green) (75%)	CLS	80.48	66.23	74.15	63.31	67.74	61.49	49.57	51.40	35.92	40.38
	SUnSAL	80.48	66.23	74.14	63.31	67.73	61.50	49.54	51.41	35.90	40.35
	FCLS	81.37	65.62	72.93	62.95	65.59	58.08	44.64	47.75	32.60	41.11
	CLSUnSAL	81.36	65.62	72.93	62.95	65.59	58.07	44.65	47.75	32.60	41.11

the pixel, there is no actual material detection observed even at the highest spatial resolution. All the detected pixels are false positives. The detection of material in the pixel is apparent when the material fraction is 1% and above. Up to 9% material fraction, the estimated abundances are strongly correlated with the spatial resolution. Beyond that, the abundances estimated are somewhat independent of spatial resolution and are closer to the actual abundances. As evident in the range of values marked green in Table 11, there is an optimal range of spatial resolution in which the estimation of abundance is possible across the

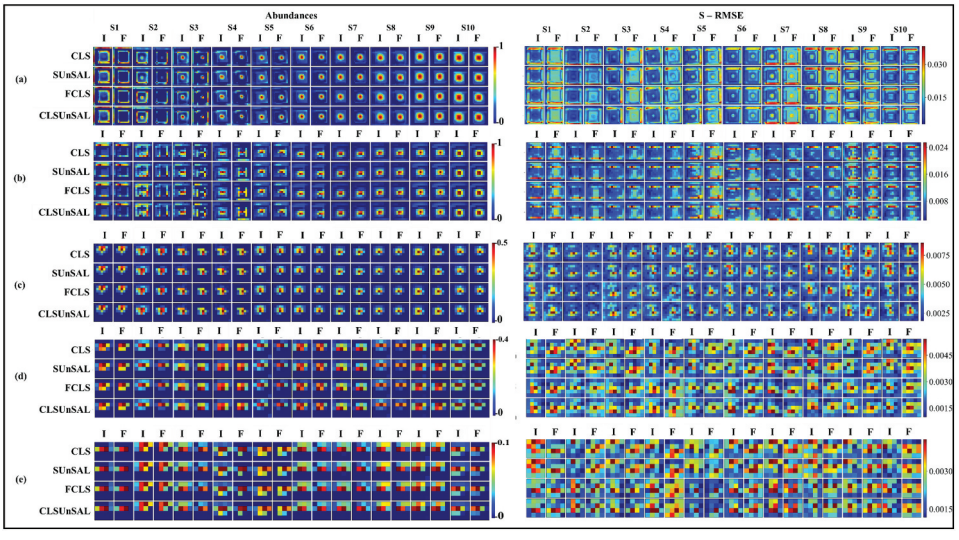

Figure 14. Estimated abundances and associated error (S – RMSE) from the spectral unmixing of the multi-resolution hyperspectral imagery ((a) 0.16 cm, (b) 0.32 cm, (c) 0.80 cm, (d) 1.61 cm, and (e) 1.99 cm) with a single background but with ten different sizes (S1 to S10) of the foreground material and from two different sources of endmembers (I: imagery; F: external spectral library).

inversion algorithms and source of endmembers. When the material fraction is up to 9%, the abundances estimated from using the external spectral library-based endmembers are relatively closer to the reference abundances. However, for the material fractions beyond 9%, the abundances from imagery derived endmembers exhibit a better match with the reference abundances. There are substantial false positives at coarser spatial resolutions independent of the inversion algorithm used and the source of endmembers.

3.4. Case-4: When the pixels has heterogenous background and the target material varies in size

The results of material abundances for the case of background composing with four different materials of equal proportion are presented in Table 12 and Figure 15. There is no trace of actual material detection when the target material's distribution within a pixel is up to 2.25%, irrespective of the source of endmembers, spatial resolution, and algorithms. The target material is detected with substantial false positives when the material fraction is 4–9% and is possible in high spatial resolution imagery and with both the sources of endmembers. Beyond the 9% proportion, the material is detected with the abundance matching reasonably closely with the reference values from both the imagery and external library-based endmembers. However, the quality of material detection, hence abundances, as evident in the form of false positives, is strongly related to spatial resolution. The variation of abundances by different inversion algorithms is marginal across the spatial resolutions and sources of endmembers.

Table 11. Summary of the estimation of material abundance (%) at the various amount of material's existence in the hyperspectral imagery. the values marked in red indicate no detection of the materials and hence are fully false positives. the values marked in orange represent the detection of the actual material fraction pixels but are largely overestimated or underestimated. Values expressed in green show the estimation of actual material abundance closely matching with the reference abundance.

Actual material fraction (%)	Inversion Algorithm	Spatial Resolution (cm)									
		0.16		0.32		0.8		1.61		1.99	
		Endmember source									
		Image	Field	Image	Field	Image	Field	Image	Field	Image	Field
0.25	CLS	5.47	2.66	5.38	3.00	10.07	5.98	18.96	8.71	14.77	6.41
	SUnSAL	5.47	2.66	5.37	3.00	10.06	5.98	18.95	8.71	14.77	6.41
	FCLS	5.14	2.74	5.30	2.85	9.41	5.95	17.51	8.69	14.30	6.36
	CLSUnSAL	5.14	2.74	5.30	2.85	9.41	5.94	17.50	8.69	14.29	6.36
1	CLS	3.75	1.24	5.65	3.02	12.06	7.01	21.54	8.30	21.85	9.14
	SUnSAL	3.75	1.24	5.65	3.02	12.06	7.01	21.54	8.30	21.85	9.14
	FCLS	2.99	1.10	4.78	2.99	11.44	6.87	20.32	7.96	21.14	9.14
	CLSUnSAL	2.99	1.10	4.78	2.99	11.44	6.87	20.31	7.96	21.13	9.14
2.25	CLS	4.69	1.97	3.96	1.66	8.63	5.03	19.21	7.40	19.74	6.91
	SUnSAL	4.69	1.97	3.96	1.66	8.63	5.03	19.20	7.40	19.74	6.91
	FCLS	4.06	1.59	3.56	1.35	7.97	5.03	17.94	7.41	19.01	6.90
	CLSUnSAL	4.06	1.59	3.56	1.35	7.97	5.03	17.94	7.41	19.01	6.90
4	CLS	6.31	2.78	6.64	3.22	9.03	5.29	21.38	9.15	22.36	7.35
	SUnSAL	6.32	2.78	6.64	3.22	9.03	5.29	21.38	9.15	22.35	7.35
	FCLS	6.07	2.39	6.37	2.84	8.48	5.29	20.19	9.08	21.69	7.32
	CLSUnSAL	6.07	2.39	6.37	2.84	8.48	5.29	20.19	9.07	21.69	7.32
6.25	CLS	10.01	4.87	10.15	5.31	15.15	9.71	20.77	8.79	22.30	9.73
	SUnSAL	10.01	4.87	10.15	5.31	15.15	9.71	20.76	8.79	22.29	9.73
	FCLS	9.78	4.57	9.65	4.95	14.39	9.70	18.84	8.77	21.20	9.75
	CLSUnSAL	9.78	4.57	9.65	4.95	14.39	9.70	18.84	8.77	21.19	9.74
9	CLS	11.66	5.95	11.23	6.59	14.92	9.51	24.33	11.37	26.14	11.35
	SUnSAL	11.66	5.95	11.23	6.59	14.92	9.51	24.32	11.37	26.13	11.35
	FCLS	11.26	5.31	10.95	6.13	14.23	9.51	22.69	11.36	24.92	11.39
	CLSUnSAL	11.26	5.31	10.95	6.13	14.22	9.51	22.68	11.35	24.92	11.39
12.25	CLS	12.27	6.68	12.13	7.85	18.12	11.85	26.36	13.04	27.68	12.39
	SUnSAL	12.27	6.68	12.13	7.85	18.12	11.85	26.35	13.04	27.68	12.39
	FCLS	11.94	5.88	11.95	7.31	17.31	11.84	24.75	13.04	26.36	12.40
	CLSUnSAL	11.94	5.88	11.95	7.31	17.31	11.83	24.75	13.04	26.35	12.40
16	CLS	17.26	10.94	16.51	10.87	18.24	11.88	24.85	10.27	27.74	12.68
	SUnSAL	17.26	10.94	16.51	10.87	18.24	11.88	24.84	10.27	27.73	12.68
	FCLS	17.03	9.70	16.38	9.74	17.45	11.87	23.19	10.27	26.72	12.72
	CLSUnSAL	17.03	9.70	16.38	9.74	17.45	11.87	23.19	10.27	26.72	12.72
20.25	CLS	22.62	14.90	22.51	15.70	25.53	16.95	36.95	19.04	31.97	16.11
	SUnSAL	22.62	14.90	22.51	15.70	25.53	16.95	36.94	19.04	31.96	16.11
	FCLS	22.07	14.36	21.89	15.57	24.32	16.91	33.85	18.94	30.06	16.07
	CLSUnSAL	22.07	14.36	21.89	15.57	24.32	16.91	33.85	18.93	30.06	16.07
25	CLS	24.19	16.34	23.22	16.57	26.57	17.81	33.52	16.85	36.41	16.60
	SUnSAL	24.19	16.34	23.21	16.57	26.57	17.81	33.52	16.85	36.40	16.60
	FCLS	23.49	14.91	23.07	15.97	25.71	17.81	31.41	16.82	34.19	16.60
	CLSUnSAL	23.49	14.91	23.07	15.97	25.71	17.81	31.40	16.82	34.19	16.60

4. Discussion

Spectral unmixing has been a widely studied and yet relatively least understood domain of remote sensing application. Originally designed as a strategy for sub-pixel classification of coarse resolution multispectral imagery, the spectral unmixing has been studied from various aspects such as its application potential, nature of signal mixing, inversion

Table 12. Summary of the estimation of material abundance (%) at the various amount of material's existence in the hyperspectral imagery. the Values marked in red indicate no detection of the materials and hence are fully false positives. the values marked in orange represent the detection of pixels of the actual material fraction but are largely overestimated or underestimated. Values represented in green show the estimation of actual material abundance closely matching with the reference abundance (endmembers: Image – from the imagery; Field – from the external spectral library).

Actual material fraction (%)	Inversion Algorithm	Spatial Resolution (cm)									
		0.16		0.32		0.8		1.61		1.99	
		Endmember source									
		Image	Field	Image	Field	Image	Field	Image	Field	Image	Field
0.25	CLS	4.44	5.01	9.18	11.05	34.02	21.79	39.92	13.93	43.53	20.23
	SUnSAL	4.44	5.00	9.18	11.04	34.03	21.80	39.99	13.93	43.59	20.24
	FCLS	4.28	5.27	8.80	12.05	40.20	21.55	53.86	19.19	50.36	23.24
	CLSUnSAL	4.28	5.27	8.79	12.05	40.19	21.54	53.87	19.20	50.43	23.24
1	CLS	4.71	4.41	10.05	11.76	33.79	18.13	40.59	20.07	42.89	18.52
	SUnSAL	4.71	4.41	10.04	11.75	33.81	18.14	40.63	20.07	42.96	18.51
	FCLS	4.62	5.39	7.48	12.20	38.15	18.15	53.94	20.03	49.47	19.29
	CLSUnSAL	4.62	5.39	7.47	12.20	38.15	18.15	53.93	20.03	49.47	19.27
2.25	CLS	6.74	6.74	13.03	14.74	32.86	18.48	44.21	22.67	52.18	24.27
	SUnSAL	6.75	6.74	13.04	14.74	32.88	18.49	44.26	22.68	52.20	24.33
	FCLS	6.42	9.44	13.14	14.55	35.64	17.21	53.64	23.31	55.57	27.54
	CLSUnSAL	6.42	9.43	13.13	14.54	35.65	17.21	53.66	23.31	55.56	27.54
4	CLS	8.19	8.20	9.96	15.13	36.97	23.17	53.17	28.41	46.71	23.11
	SUnSAL	8.20	8.20	9.97	15.13	37.02	23.19	53.19	28.45	46.77	23.10
	FCLS	7.70	11.03	9.62	14.99	40.87	21.00	62.07	28.60	59.10	22.07
	CLSUnSAL	7.70	11.03	9.61	14.99	40.87	20.99	62.10	28.60	59.14	22.08
6.25	CLS	7.74	7.07	12.99	12.26	38.47	24.97	49.10	25.43	50.90	27.47
	SUnSAL	7.75	7.07	12.99	12.25	38.50	24.98	49.15	25.45	50.99	27.49
	FCLS	7.49	6.71	12.20	10.49	45.80	24.10	58.77	29.84	61.17	27.84
	CLSUnSAL	7.49	6.70	12.20	10.49	45.79	24.10	58.76	29.83	61.24	27.84
9	CLS	8.50	7.55	14.40	15.34	37.38	21.94	54.14	22.69	50.66	18.55
	SUnSAL	8.50	7.55	14.41	15.34	37.41	21.95	54.21	22.72	50.82	18.56
	FCLS	8.13	7.06	13.65	15.09	40.87	21.69	64.80	27.10	63.25	21.48
	CLSUnSAL	8.12	7.05	13.65	15.08	40.88	21.69	64.82	27.11	63.28	21.48
12.25	CLS	9.80	8.88	16.73	15.71	44.67	28.20	50.67	29.44	54.44	29.09
	SUnSAL	9.80	8.88	16.73	15.71	44.69	28.21	50.71	29.46	54.46	29.12
	FCLS	9.72	8.89	16.29	16.15	48.97	27.26	59.35	29.60	62.92	30.39
	CLSUnSAL	9.72	8.89	16.28	16.15	48.98	27.27	59.37	29.61	62.96	30.37
16	CLS	14.89	12.56	17.78	17.86	40.47	25.82	57.85	32.61	53.99	29.01
	SUnSAL	14.89	12.56	17.78	17.85	40.48	25.83	57.91	32.62	54.06	29.00
	FCLS	14.48	13.53	16.80	17.09	43.26	25.15	68.87	32.10	65.81	26.94
	CLSUnSAL	14.48	13.53	16.79	17.09	43.27	25.15	68.85	32.12	65.85	26.95
20.25	CLS	20.09	16.25	21.76	23.08	41.26	26.74	58.20	29.93	49.25	29.78
	SUnSAL	20.10	16.26	21.77	23.08	41.30	26.75	58.23	29.94	49.26	29.77
	FCLS	19.35	17.35	19.05	20.78	45.12	24.89	61.67	32.15	59.22	28.96
	CLSUnSAL	19.35	17.35	19.04	20.77	45.15	24.89	61.69	32.15	59.22	28.94
25	CLS	20.12	16.73	27.80	26.09	43.95	28.03	57.50	31.71	56.12	28.80
	SUnSAL	20.13	16.74	27.81	26.10	43.98	28.04	57.52	31.74	56.20	28.83
	FCLS	19.89	17.44	26.64	25.42	48.42	26.76	65.31	35.04	62.46	31.59
	CLSUnSAL	19.89	17.44	26.63	25.42	48.43	26.76	65.31	35.04	62.54	31.62

algorithms, constraints, and propagation errors. Hyperspectral imagery has helped resolve some critical theoretical limitations of multispectral imagery and has renewed research on spectral unmixing. Spatial quantification of various sub-pixel constituents is expected to be the primary application of the spectral unmixing of hyperspectral imagery. Several studies have reported the potential of spectral unmixing of high-resolution hyperspectral imagery in agriculture (Bioucas-Dias et al. 2013; Lu et al. 2020; Salehani, Arabnejad and Gazor 2021;

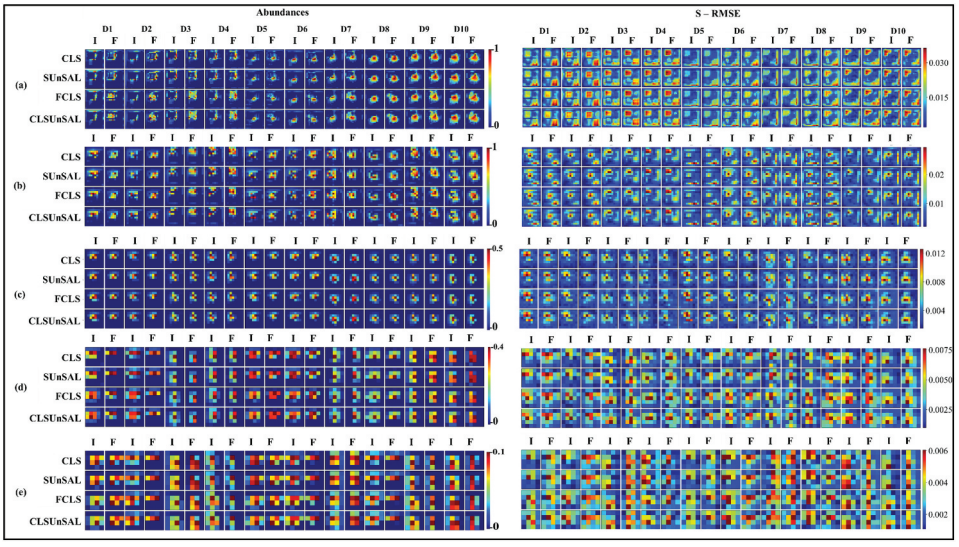

Figure 15. Estimated abundances and error scores (S – RMSE) retrieved from the spectral unmixing of multi-resolution hyperspectral imagery ((a) 0.16 cm; (b) 0.32 cm; (c) 0.80 cm; (d) 1.61 cm; (e) 1.99 cm) containing heterogeneous background and a single foreground material at different spatial size distributions (D1 to D10). Unmixing was performed using four different inversion algorithms (CLS, SUnSAL, FCLS, CLSUnSAL) using two different sources of endmembers (I: imagery; F: external spectral library).

Zhu et al. 2021), mineralogy (Hong et al. 2019; Koirala et al. 2019), environmental monitoring (Siu, Traish and Da Xu 2021; Wang et al. 2021; Zheng et al. 2021), food quality assessment (Badaró et al. 2021), and medical diagnostics (Bench and Cox 2021; Wirth et al. 2021). Despite its potential application as a broad-based analytical approach in remote sensing, several fundamental questions and challenges are yet to be dealt with to make headway. Attempting to address the spectral abundance estimation issues from the linear versus non-linear perspective, the dominant body of literature deals with optional pre-processing stages such as dimensionality, algorithms for endmember extraction, complicated inversion algorithms, and computational approaches. Most works have used standard satellite or airborne datasets and simulated imagery, considering the extensively distributed land use/cover categories as candidate materials for abundance estimations. The non-availability of unmixing-specific real-world benchmark datasets in the public domain has been one of the major impediments in pursuing research on spectral unmixing of hyperspectral imagery from a realistic perspective. This work has studied some vital issues in material abundance estimations in hyperspectral imagery from a solution-driven empirical approach and has contributed open-source high-resolution benchmark datasets for spectral unmixing. The experimental implementations assessing the magnitude and change of abundances as a function of spatial resolution, number of composing materials, size and orientation of materials, source of endmembers, and background are carried out on the benchmark datasets acquired. We discuss objectively the key parameters, features, results, and implications in the following sub-sections.

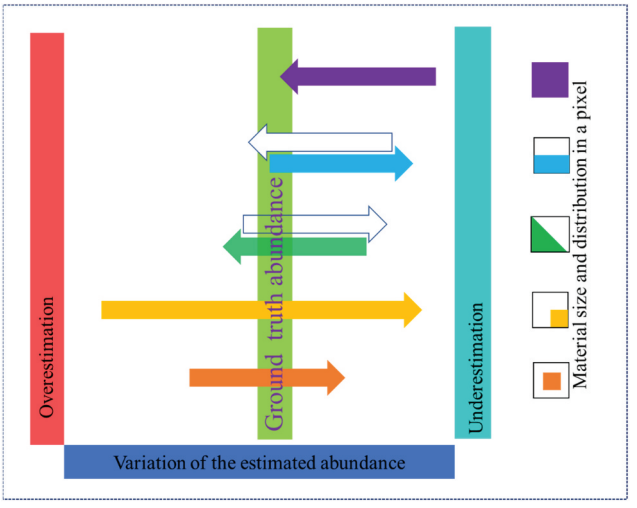

Figure 16. Amount of abundance estimated form high spatial resolution (arrow-head) to coarser (arrow-tail) spatial resolution for different material distribution.

4.1. Impact of spatial resolution

Although unmixing is considered a spectral problem to solve for material abundances in coarse resolution imagery, the substantial range of spatial resolutions for a material of fixed spatial distribution introduces a multitude of uncertainties by the quality of endmembers, background-material interactions, and geometric factors. Contrary to the current notion of linear reduction of abundance due to decreasing spatial resolution (Li et al. 2011; Ghasrodashti et al. 2017), the results show a different pattern. The change of material abundances due to decreasing spatial resolution indicates three different possibilities: (i) there is only marginal to no change, (ii) linearly decreasing (underestimation), and (iii) non-linear, wherein both the overestimation and underestimation are observed. The possible case is influenced by the material type and source of endmembers. While, in many instances, there is a consistent decrease in the abundances estimated (underestimation), there are instances, especially when there are relatively more materials composed, in which the abundances are overestimated. The changes in abundances may be due to the increased background complexity and illumination geometry. This observation suggests that there is a necessity of optimising the spatial resolution concerning the specific material(s) of interest by spectral unmixing.

4.2. Source of endmembers

Central to the spectral unmixing problem, endmembers and the related parameters – number of endmembers, source, and identification method, control the possibility and quality of abundance retrievals. Thanks to the full spectrum measurement of material's radiance in hyperspectral data, the estimation and location of endmembers for further consumption in spectral unmixing has been extensively studied (Somers et al. 2012;

Drumetz et al. 2019; Xu, Du and Fan 2019). Two parameters related to endmembers – the number of endmembers and the source of endmembers are decisive in the validity of abundances estimated. Partially supporting the previous observations (Bioucas-Dias et al. 2012), imagery-derived endmembers offer abundance estimates consistently closer to the ground truth abundance. Compared to the estimates from imagery-derived endmembers, the estimates obtained from using the external spectral library as the source of endmembers are consistently lower. However, the absolute value of the abundances retrieved from using the external spectral library is 70% to 80% of the ground truth value indicating the promise of using reference spectral libraries as sources of endmembers. Further, compared to the imagery-derived endmembers, the variation of abundances as a function of spatial resolution is relatively low. Based on the observed magnitude and the stability of abundances estimated from using the external library as the source of endmembers, developing spectral knowledge-based methods seem possible (Baldridge et al. 2009; Meerdink et al. 2019), thereby enabling large-scale spectral unmixing tasks.

4.3. *Influence of the type and number of materials*

The abundances estimated are strongly influenced by the type of material, the number of materials, and their orientation. When there was only one material, the difference between the estimated and ground truth abundance was negligible (0.07%; green material) to substantial (20%; violet material) and maintained a similar trend across different spatial resolutions (Table 5). When there are two materials in the spectrum, the quality of the estimated abundance compared to the ground measured abundance is controlled by three factors – the type of material, orientation, and the spatial fraction of the material. Overall, the abundance difference is marginal (1.2%; blue material) to substantial (7%; red material). If the spatial orientation of the material is diagonal, then the difference of abundance is reduced marginally to 5%, and there is no noticeable difference between the abundances of different materials. If the two materials have substantial different fractions, e.g. 25% and 75%, the estimated abundances are overestimated as the spatial resolution decreases (see Table 10). The specific location of the smaller-fraction material in the pixel also influences the abundance. Estimated abundances of the material fraction located at the corner of a pixel are relatively closer to the ground truth abundance. Material fractions at the center of a pixel are substantially overestimated at the coarser spatial resolutions (see Tables 10 and 11 (20.25%)). Further, as the spatial resolution becomes coarser, the difference of the estimated and ground truth abundances is negligible for a few materials. When there are three materials with different spatial fractions, there is a general trend of underestimation of the abundances. The larger material fraction exhibits relatively higher underestimation (about 12%) compared to the materials of smaller fraction (about 2.5%). If there are four materials in the pixel spectrum with equal spatial fractions, the estimated abundances exhibit a complex pattern wherein some materials are overestimated at the higher spatial resolution. As the spatial resolution becomes coarser, the same materials are substantially underestimated. This indicates the material-specific nature of the spectral unmixing. Lack of distinct spectral features reduces the inter-material

contrast and induces pseudo-background, which may be the primary factor responsible for this pattern. Overall, as the number of materials in a pixel spectrum increases, there is a general trend of overestimation of the abundances for most of the materials at the cost of substantial reduction of the abundance for a material that lacks distinct spectral features.

4.4. Spatial size, orientation and background complexity

The quality of material detection and the corresponding abundances vary substantially by the spatial size of the material. Three different possibilities are observed for the estimated abundances: no detection at all, detection with substantial false positives, and detection with a closer match with the ground truth abundance. Summary of the observations on the variation of the estimated abundance pertaining to material size and distribution within a pixel, as the spatial resolution varies, is visualized in Figure 16. The quality of abundances estimated is substantially influenced by the positioning and size of material in a hyperspectral pixel. The direction of change indicated by overestimation or underestimation is controlled by the spatial resolution.

The minimum threshold fraction that material should distribute in the ground sampling distance for detection is varied by the nature of the local background. If the imagery is acquired with a homogenous local background, then a material with at least 1% spatial extent in the pixel is detected. If the local background is heterogenous, then the minimum threshold increases to 4%. In both the cases of backgrounds, there are substantial false positives until the spatial size of the material is up to 9%. Beyond this, the material is detected without any false positives and the estimated abundance is closer to the ground measured abundance. However, the estimated abundances are strongly influenced by the spatial resolution and are linearly overestimated with the decreasing spatial resolution. Apart from the size of the material, the relative orientation also influences the quality of abundance. The cross-positioned material fractions are estimated better compared to the parallel-positioned material (see Figure 12 and Table 9).

4.5. Algorithms

Compared to the generation of benchmark datasets specific to spectral unmixing, most of the studies during the last two decades have focused on the pre-processing and inversion algorithms. Variants of non-linear and sparse modeling-based approaches have been extensively reported. While the broad perspective of linear vs non-linear spectral mixture is widely discussed, most practical approaches for spectral unmixing consider linear spectral mixing. Considering the influence of algorithms on the retrieval quality of abundances under different cases of the material-endmember-spatial resolution continuum, the results have been analyzed for the patterns of changes in the abundances as a function of inversion algorithms. Results indicate that, at the finer spatial resolutions, the difference in abundances across the different inversion algorithms is marginal (about 2%) and is less than the inter-material changes. In contrast, at the coarser spatial resolution, the changes in abundances from constrained (CLS) and fully constrained (FCLS) inversion algorithms

are substantial (about 3% to 5%) and are comparable to that of inter-material abundance changes. Results from the sparse and non-sparse inversion algorithms are similar across the materials, spatial resolutions, and sources of endmembers. This observation supports the premise that reference spectral libraries can be used as sources of endmembers (Baldridge et al. 2009; Meerdink et al. 2019) for potential operational and knowledge transfer-based spectral unmixing across different application domains.

4.6. Method of validating the material abundances

As a measure of validation in spectral unmixing, analogous to a reverse engineering problem, the estimated abundances and endmembers are used to reconstruct spectra for further comparison with the original spectra. Popularly known as the signal-to-reconstruction error (SRE) (Jiang et al. 2018), the metric quantifies the bulk of spectral magnitudes considering the broad-based spectral features and the spatially continuous abundances in the ground sampling distance. As a result, assessment of the quality of abundance is indirect and is ambiguous in that only pixel's spectral characterization in a few spatial-spectral combinations is reflected. The SRE does not map the footprint of the estimated abundances to the actual abundances. Therefore, the validation of spectral unmixing is indicated by statistical comparison of the reconstructed pixel with the original pixel, and the explicit comparison of the estimated abundances vis-à-vis actual abundances is not possible. As evident across the different scenarios of abundance estimations in this work, the quality of reconstructed spectra is outstanding, thus theoretically suggesting the closer matching of estimated and actual abundances. However, there have been substantial differences in the actual and estimated abundances in multiple cases of spectral unmixing scenarios considered. Results point out that reflectance spectra can be reconstructed mathematically by various ways of combining the base spectra of a material. We, therefore, suggest using direct area-based abundance validation metrics such as the relative areal fraction used in this study.

This study was undertaken considering the fundamental nature of material-radiation interactions and the relevance of differential spectral features across different materials. The experiments are implemented on various datasets of hyperspectral imagery acquired in natural illumination settings representing different material types, sources of endmembers, and spatial resolutions. There may be some uncertainties in the imaging-geometry driven abundances due to residual uncontrollable rapid-changes in solar illumination and mechanical movements of the platform. Nevertheless, the quality of data acquisitions and the general nature of experimental strategies met to such as extent that these residual limitations would not alter the interpretation and observations. While the results elucidate some critical aspects of spectral unmixing unaddressed so far, care should be exercised while extrapolating the observations to experiments on remote sensing data from aerial and satellite platforms. We recommend further studies on the non-linear nature of the object-space and the likely impact of geometric and radiometric inconsistencies through drone, airborne or satellite hyperspectral imaging. The benchmark datasets acquired with corresponding ground truth data are available for public access.

5. Conclusions

The impact of various vital parameters of imaging-space and material-space for material-abundance using spectral unmixing has been assessed. To advance the state-of-the-art benchmark studies, we acquired multi-resolution hyperspectral datasets with point-to-point ground truth measurements of materials' abundances and implemented spectral unmixing from various perspectives. Demonstrating the proof-of-concept on abundance estimations from a reference level, the results imply some new insights on the spectral unmixing problem in general, as stated below.

- Unambiguous estimation of material abundance is possible if the magnitude of the material distribution is at least 1% in the pixel.
- Easing the complex process of endmember detection in the imagery, results suggest that an external spectral library can be a functional source of endmembers. The error-accuracy estimates are comparable to that of the imagery-based endmembers.
- Compared to the substantial variations observed with the results from imagery-based endmembers, the magnitude of material abundances obtained from in-situ spectral library-based endmembers is stable across different spatial resolutions.
- Contrary to the belief that spectral unmixing is for coarser-resolution remote sensing imagery, results indicate that material abundances vary substantially by spatial resolution and that there is an optimal spatial resolution for different types of pixel composition, the number of materials, relative spatial distribution, and spectral distinctness compared to the background.
- The variations in the performance of different inversion algorithms are not substantial, and the simplified sparse algorithms offer a similar level of abundance retrievals.

The benchmark datasets will be valuable resources for the research community for studying spectral unmixing from different scenario-based and methodological perspectives.

Acknowledgements

This research was funded by Department of Science and Technology, Government of India (Grant Number: BDID/01/23/2014-HSRS/37) as part of the Network Programme on Imaging Spectroscopy and Applications (NISA).

We gratefully acknowledge the anonymous reviewer for constructive criticism and helpful comments and suggestions.

Disclosure statement

No potential conflict of interest was reported by the author(s).

REFERENCES

Adão, T., J. Hruška, L. Pádua, J. Bessa, E. Peres, R. Morais, and J. Sousa. 2017. "Hyperspectral Imaging: A Review on UAV-Based Sensors, Data Processing and Applications for Agriculture and Forestry." *Remote Sensing* 9 (11): 1110. doi:10.3390/rs9111110.

Badaró, A. T., J. M. Amigo, J. Blasco, N. Aleixos, A. R. Ferreira, M. T. P. S. Clerici, and D. F. Barbin. 2021. "Near Infrared Hyperspectral Imaging and Spectral Unmixing Methods for Evaluation of Fiber Distribution in Enriched Pasta." *Food Chemistry* 343 (May): 128517. doi:10.1016/j.foodchem.2020.128517.

Baldridge, A. M., S. J. Hook, C. I. Grove, and G. Rivera. 2009. "The ASTER Spectral Library Version 2.0." *Remote Sensing of Environment* 113 (4): 711. doi:10.1016/j.rse.2008.11.007.

Bench, C. and B. Cox. 2021. "Quantitative Photoacoustic Estimates of Intervascular Blood Oxygenation Differences Using Linear Unmixing." *Journal of Physics. Conference Series* 1761 (January): 12001. doi:10.1088/1742-6596/1761/1/012001.

Bioucas-Dias, J. M. 2009. "A Variable Splitting Augmented Lagrangian Approach to Linear Spectral Unmixing." 2009 First Workshop on Hyperspectral Image and Signal Processing: Evolution in Remote Sensing, 1. Grenoble: IEEE. doi:10.1109/WHISPERS.2009.5289072.

Bioucas-Dias, J. M. and M. A. T. Figueiredo. 2010. "Alternating Direction Algorithms for Constrained Sparse Regression: Application to Hyperspectral Unmixing." 2010 2nd Workshop on Hyperspectral Image and Signal Processing: Evolution in Remote Sensing, 1. Reykjavik, Iceland: IEEE. doi:10.1109/WHISPERS.2010.5594963.

Bioucas-Dias, J. M., A. Plaza, G. Camps-Valls, P. Scheunders, N. Nasrabadi, and J. Chanussot. 2013. "Hyperspectral Remote Sensing Data Analysis and Future Challenges." *IEEE Geoscience and Remote Sensing Magazine* 1 (2): 6. doi:10.1109/MGRS.2013.2244672.

Bioucas-Dias, J. M., A. Plaza, N. Dobigeon, M. Parente, Q. Du, P. Gader, and J. Chanussot. 2012. "Hyperspectral Unmixing Overview: Geometrical, Statistical, and Sparse Regression-Based Approaches." *IEEE Journal of Selected Topics in Applied Earth Observations and Remote Sensing* 5 (2): 354. doi:10.1109/JSTARS.2012.2194696.

Borsoi, R. A., T. Imbiriba, and J. C. M. Bermudez. 2020a. "Deep Generative Endmember Modeling: An Application to Unsupervised Spectral Unmixing." *IEEE Transactions on Computational Imaging* 6: 374. doi:10.1109/TCI.2019.2948726.

Borsoi, R. A., T. Imbiriba, J. C. M. Bermudez, and C. Richard. 2020b. "A Blind Multiscale Spatial Regularization Framework for Kernel-Based Spectral Unmixing." *IEEE Transactions on Image Processing* 29: 4965. doi:10.1109/TIP.2020.2978342.

Bullock, E. L., C. E. Woodcock, and P. Olofsson. 2020. "Monitoring Tropical Forest Degradation Using Spectral Unmixing and Landsat Time Series Analysis." *Remote Sensing of Environment* 238 (March): 110968. doi:10.1016/j.rse.2018.11.011.

Cardoso-Fernandes, J., J. Silva, A. Lima, A. C. Teodoro, M. Perrotta, J. Cauzid, and E. Roda-Robles. 2020. "Characterization of Lithium (Li) Minerals from the Fregeneda-Almendra Region Through Laboratory Spectral Measurements: A Comparative Study." In *Earth Resources and Environmental Remote Sensing/gis Applications XI*, edited by K. Schulz; K. G. Nikolakopoulos, and U. Michel. Bellingham, USA: SPIE, 20.

Cerra, D., M. Pato, K. Alonso, C. Köhler, M. Schneider, R. de Los Reyes, E. Carmona, et al. 2021. "DLR HySu—a Benchmark Dataset for Spectral Unmixing." *Remote Sensing* 13 (13): 2559. doi:10.3390/rs13132559.

Chabrillat, S., A. Gholizadeh, C. Neumann, D. Berger, R. Milewski, Y. Ogen, and E. Ben-Dor. 2019. "Preparing a Soil Spectral Library Using the Internal Soil Standard (ISS) Method: Influence of Extreme Different Humidity Laboratory Conditions." *Geoderma* 355 (December): 113855. doi:10.1016/j.geoderma.2019.07.013.

Cheng, X., Z. Cai, J. Li, M. Wen, Y. Wang, and D. Zeng. 2021. "A Spatial-Spectral Clustering-Based Algorithm for Endmember Extraction and Hyperspectral Unmixing." *International Journal of Remote Sensing* 42 (5): 1948. doi:10.1080/01431161.2020.1849851.

Drumetz, L., J. Chanussot, and C. Jutten. 2020. "Spectral Unmixing: A Derivation of the Extended Linear Mixing Model from the Hapke Model." *IEEE Geoscience and Remote Sensing Letters* 17 (11): 1866. doi:10.1109/LGRS.2019.2958203.

Drumetz, L., T. R. Meyer, J. Chanussot, A. L. Bertozzi, and C. Jutten. 2019. "Hyperspectral Image Unmixing with Endmember Bundles and Group Sparsity Inducing Mixed Norms." *IEEE Transactions on Image Processing* 28 (7): 3435. doi:10.1109/TIP.2019.2897254.

Eismann, M. T. 2012. *Hyperspectral Remote Sensing*. Bellingham, Wash: SPIE Press.

Feng, S. and F. Fan. 2021. "Analyzing the Effect of the Spectral Interference of Mixed Pixels Using Hyperspectral Imagery." *IEEE Journal of Selected Topics in Applied Earth Observations and Remote Sensing* 14: 1434. doi:10.1109/JSTARS.2020.3045712.

Feng, R., L. Wang, and Y. Zhong. 2019. "Local Block Grouping with Napca Spatial Preprocessing for Hyperspectral Remote Sensing Imagery Sparse Unmixing." IGARSS 2019 - 2019 IEEE International Geoscience and Remote Sensing Symposium, 556. Yokohama, Japan: IEEE. doi:10.1109/IGARSS.2019.8900627.

Ghasrodashti, E., A. Karami, R. Heylen, and P. Scheunders. 2017. "Spatial Resolution Enhancement of Hyperspectral Images Using Spectral Unmixing and Bayesian Sparse Representation." *Remote Sensing* 9 (6): 541. doi:10.3390/rs9060541.

Gruninger, J. H., A. J. Ratkowski, and M. L. Hoke. 2004. "The Sequential Maximum Angle Convex Cone (SMACC) Endmember Model." In edited by S. S. Shen and P. E. Lewis, 1. Orlando, FL. doi:10.1117/12.543794.

Hannula, H.-R., K. Heinilä, K. Böttcher, O.-P. Mattila, M. Salminen, and J. Pulliainen. 2020. "Laboratory, Field, Mast-Borne and Airborne Spectral Reflectance Measurements of Boreal Landscape During Spring." *Earth System Science Data* 12 (1): 719. doi:10.5194/essd-12-719-2020.

Heylen, R., V. Andrejchenko, Z. Zahiri, M. Parente, and P. Scheunders. 2019. "Nonlinear Hyperspectral Unmixing with Graphical Models." *IEEE Transactions on Geoscience and Remote Sensing* 57 (7): 4844. doi:10.1109/TGRS.2019.2893489.

Hong, D., N. Yokoya, J. Chanussot, and X. X. Zhu. 2019. "An Augmented Linear Mixing Model to Address Spectral Variability for Hyperspectral Unmixing." *IEEE Transactions on Image Processing* 28 (4): 1923. doi:10.1109/TIP.2018.2878958.

Hou, W., Y. Mao, C. Xu, Z. Li, D. Li, Y. Ma, and H. Xu. 2019. "Study on the Spectral Reconstruction of Typical Surface Types Based on Spectral Library and Principal Component Analysis." In *Fifth Symposium on Novel Optoelectronic Detection Technology and Application*, edited by Q. Yu; W. Huang, and Y. He, 170. Xi'an, China: SPIE. doi:10.1117/12.2521743.

Hua, Z., X. Li, J. Jiang, and L. Zhao. 2021. "Gated Autoencoder Network for Spectral–spatial Hyperspectral Unmixing." *Remote Sensing* 13 (16): 3147. doi:10.3390/rs13163147.

Iordache, M.-D., J. M. Bioucas-Dias, and A. Plaza. 2011. "Sparse Unmixing of Hyperspectral Data." *IEEE Transactions on Geoscience and Remote Sensing* 49 (6): 2014. doi:10.1109/TGRS.2010.2098413.

Iordache, M.-D., J. M. Bioucas-Dias, and A. Plaza. 2014. "Collaborative Sparse Regression for Hyperspectral Unmixing." *IEEE Transactions on Geoscience and Remote Sensing* 52 (1): 341. doi:10.1109/TGRS.2013.2240001.

Janik, L. J., J. M. Soriano-Disla, and S. T. Forrester. 2020. "Feasibility of Handheld Mid-Infrared Spectroscopy to Predict Particle Size Distribution: Influence of Soil Field Condition and Utilisation of Existing Spectral Libraries." *Soil Research* 58 (6): 528. doi:10.1071/SR20097.

Jiang, X., Gong, M., Li, H., Zhang, M., & Li, J. 2018. "A two-phase multi-objective sparse unmixing approach for hyperspectral data". *IEEE Transactions on Geoscience and Remote Sensing* 56 (1): 508–523.

Jin, Q., Y. Ma, X. Mei, X. Dai, H. Li, F. Fan, and J. Huang. 2019. "Gaussian Mixture Model for Hyperspectral Unmixing with Low-Rank Representation." IGARSS 2019 - 2019 IEEE International Geoscience and Remote Sensing Symposium, 294. Yokohama, Japan: IEEE. doi:10.1109/IGARSS.2019.8898410.

Keshava, N. 2003. "A Survey of Spectral Unmixing Algorithms." *Lincoln Laboratory Journal* 14 (1): 55.

Keshava, N. and J. F. Mustard. 2002. "Spectral Unmixing." *IEEE Signal Processing Magazine* 19 (1): 44. doi:10.1109/79.974727.

Kizel, F. and J.A. Benediktsson. 2020. "Spatially Enhanced Spectral Unmixing Through Data Fusion of Spectral and Visible Images from Different Sensors." *Remote Sensing* 12 (8): 1255. doi:10.3390/rs12081255.

Koirala, B., M. Khodadadzadeh, C. Contreras, Z. Zahiri, R. Gloaguen, and P. Scheunders. 2019. "A Supervised Method for Nonlinear Hyperspectral Unmixing." *Remote Sensing* 11 (20): 2458. doi:10.3390/rs11202458.

Li, Z., Y. Altmann, J. Chen, S. Mclaughlin, and S. Rahardja. 2021. "Sparse Linear Spectral Unmixing of Hyperspectral Images Using Expectation-Propagation." *ArXiv:2106.09985 [Eess, Stat]*, June. http://arxiv.org/abs/2106.09985 .

Li, Z., J. Chen, and S. Rahardja. 2019. "Kernel-Based Nonlinear Spectral Unmixing with Dictionary Pruning." *Remote Sensing* 11 (5): 592. doi:10.3390/rs11020122.

Li, C., Y. Liu, J. Cheng, R. Song, H. Peng, Q. Chen, and X. Chen. 2018. "Hyperspectral Unmixing with Bandwise Generalized Bilinear Model." *Remote Sensing* 10 (10): 1600. doi:10.3390/rs10101600.

Li, Y., W.-K. Ma, and N. D. Sidiropoulos. 2021. "Robust Probabilistic Simplex Component Analysis." 2021 IEEE Statistical Signal Processing Workshop (SSP), 456. Rio de Janeiro, Brazil: IEEE. doi:10.1109/SSP49050.2021.9513843.

Li, X., Tian, L., Zhao, X., & Chen, X. 2011. "A super resolution approach for spectral unmixing of remote sensing images". *International journal of remote sensing* 32 (21): 6091–6107.

Liu, H., Y. Lu, Z. Wu, Q. Du, J. Chanussot, and Z. Wei. 2021. "Bayesian Unmixing of Hyperspectral Image Sequence with Composite Priors for Abundance and Endmember Variability." IEEE Transactions on Geoscience and Remote Sensing, 1. doi:10.1109/TGRS.2021.3064708.

Lu, B., P. Dao, J. Liu, Y. He, and J. Shang. 2020. "Recent Advances of Hyperspectral Imaging Technology and Applications in Agriculture." *Remote Sensing* 12 (16): 2659. doi:10.3390/rs12162659.

Meerdink, S. K., S. J. Hook, D. A. Roberts, and E. A. Abbott. 2019. "The ECOSTRESS Spectral Library Version 1.0." *Remote Sensing of Environment* 230 (September): 111196. doi:10.1016/j.rse.2019.05.015.

Mishra, G., H. Govil, and P. K. Srivastava. 2021. "Identification of Malachite and Alteration Minerals Using Airborne AVIRIS-NG Hyperspectral Data." *Quaternary Science Advances* 4 (October): 100036. doi:10.1016/j.qsa.2021.100036.

Nascimento, J. M. P. and J. M. B. Dias. 2005. "Vertex Component Analysis: A Fast Algorithm to Unmix Hyperspectral Data." *IEEE Transactions on Geoscience and Remote Sensing* 43 (4): 898. doi:10.1109/TGRS.2005.844293.

Nascimento, J. and G. Martín. 2020. "Nonlinear Spectral Unmixing." *Data Handling in Science and Technology* 32: 151. Elsevier. doi:10.1016/B978-0-444-63977-6.00008-0.

Nidamanuri, R. R. and B. Zbell. 2013. "Understanding the Unique Spectral Signature of Winter Rape." *Journal of the Indian Society of Remote Sensing* 41 (1): 57. doi:10.1007/s12524-012-0211-x.

Palsson, B., J. Sigurdsson, J. R. Sveinsson, and M. O. Ulfarsson. 2018. "Hyperspectral Unmixing Using a Neural Network Autoencoder." *IEEE Access* 6: 25646. doi:10.1109/ACCESS.2018.2818280.

Palsson, B., J. R. Sveinsson, and M. O. Ulfarsson. 2019. "Multitask Learning for Spatial-Spectral Hyperspectral Unmixing." IGARSS 2019 - 2019 IEEE International Geoscience and Remote Sensing Symposium, 564. Yokohama, Japan: IEEE. doi:10.1109/IGARSS.2019.8900229.

Park, J.-J., K.-A. Park, P.-Y. Foucher, P. Deliot, S. L. Floch, T.-S. Kim, S. Oh, and M. Lee. 2021. "Hazardous Noxious Substance Detection Based on Ground Experiment and Hyperspectral Remote Sensing." *Remote Sensing* 13 (2): 318. doi:10.3390/rs13020318.

Plaza, A. and C.-I. Chang. 2005. "Fast Implementation of Pixel Purity Index Algorithm." In edited by S. S. Shen and P. E. Lewis, 307. Orlando, Florida, USA. doi:10.1117/12.602374.

Qi, J., Z. Gong, W. Xue, X. Liu, A. Yao, and P. Zhong. 2021. "An Unmixing-Based Network for Underwater Target Detection from Hyperspectral Imagery." *IEEE Journal of Selected Topics in Applied Earth Observations and Remote Sensing* 14: 5470. doi:10.1109/JSTARS.2021.3080919.

Qi, X., Z. Ling, J. Zhang, J. Chen, H. Cao, C. Liu, L. Qiao, et al. 2020. "Photometric Normalization of Chang'e-4 Visible and Near-Infrared Imaging Spectrometer Datasets: A Combined Study of in-Situ and Laboratory Spectral Measurements." *Remote Sensing* 12 (19): 3211. doi:10.3390/rs12193211.

Salehani, Y. E., E. Arabnejad, and S. Gazor. 2021. "Augmented Gaussian Linear Mixture Model for Spectral Variability in Hyperspectral Unmixing." ICASSP 2021 - 2021 IEEE International Conference on Acoustics, Speech and Signal Processing (ICASSP), 1880–1884. Toronto, ON, Canada: IEEE. doi:10.1109/ICASSP39728.2021.9414358.

Savitzky, A. and M. J. E. Golay. 1964. "Smoothing and Differentiation of Data by Simplified Least Squares Procedures." *Analytical Chemistry* 36 (8): 1627. doi:10.1021/ac60214a047.

Shah, D. and T. Zaveri. 2019. "Hyperspectral Endmember Extraction Using Band Quality." 2019 IEEE 16th India Council International Conference (INDICON), 1. Rajkot, India: IEEE. doi:10.1109/INDICON47234.2019.9029064.

Shi, Z., T. Shi, M. Zhou, and X. Xu. 2018. "Collaborative Sparse Hyperspectral Unmixing Using l_{0} Norm." *IEEE Transactions on Geoscience and Remote Sensing* 56 (9): 5495. doi:10.1109/TGRS.2018.2818703.

Siu, C., J. Traish, and R. Y. Da Xu. 2021. "Greedy UnMixing for Q-Learning in Multi-Agent Reinforcement Learning." ArXiv:2109.09034 [Cs, Stat], September. http://arxiv.org/abs/2109.09034 .

Somers, B., M. Zortea, A. Plaza, and G. P. Asner. 2012. "Automated Extraction of Image-Based Endmember Bundles for Improved Spectral Unmixing." *IEEE Journal of Selected Topics in Applied Earth Observations and Remote Sensing* 5 (2): 396. doi:10.1109/JSTARS.2011.2181340.

Uezato, T., M. Fauvel, and N. Dobigeon. 2018. "A Multiple Endmember Mixing Model to Handle Spectral Variability in Hyperspectral Unmixing." 2018 9th Workshop on Hyperspectral Image and Signal Processing: Evolution in Remote Sensing (WHISPERS), 1. Amsterdam, Netherlands: IEEE. doi:10.1109/WHISPERS.2018.8747110.

Wang, Q., X. Ding, X. Tong, and P. M. Atkinson. 2021. "Spatio-Temporal Spectral Unmixing of Time-Series Images." *Remote Sensing of Environment* 259 (June): 112407. doi:10.1016/j.rse.2021.112407.

Wang, D., Z. Shi, and X. Cui. 2018. "Robust Sparse Unmixing for Hyperspectral Imagery." *IEEE Transactions on Geoscience and Remote Sensing* 56 (3): 1348. doi:10.1109/TGRS.2017.2761912.

Wei, L., K. Wang, Q. Lu, Y. Liang, H. Li, Z. Wang, R. Wang, and L. Cao. 2021. "Crops Fine Classification in Airborne Hyperspectral Imagery Based on Multi-Feature Fusion and Deep Learning." *Remote Sensing* 13 (15): 2917. doi:10.3390/rs13152917.

Winkler, J. R. 1993. "Numerical Recipes in C: The Art of Scientific Computing, Second Edition." *Endeavour* 17 (4): 201. doi:10.1016/0160-9327(93)90069-F.

Wirth, D., B. Byrd, B. Meng, R. R. Strawbridge, K. S. Samkoe, and S. C. Davis. 2021. "Hyperspectral Imaging and Spectral Unmixing for Improving Whole-Body Fluorescence Cryo-Imaging." *Biomedical Optics Express* 12 (1): 395. doi:10.1364/BOE.410810.

Xu, M., B. Du, and Y. Fan. 2019. "Endmember Extraction from Highly Mixed Data Using Linear Mixture Model Constrained Particle Swarm Optimization." *IEEE Transactions on Geoscience and Remote Sensing* 57 (8): 5502. doi:10.1109/TGRS.2019.2899826.

Zhang, S., J. Li, H.-C. Li, C. Deng, and A. Plaza. 2018a. "Spectral–spatial Weighted Sparse Regression for Hyperspectral Image Unmixing." *IEEE Transactions on Geoscience and Remote Sensing* 56 (6): 3265. doi:10.1109/TGRS.2018.2797200.

Zhang, S., J. Li, Z. Wu, and A. Plaza. 2018b. "Spatial Discontinuity-Weighted Sparse Unmixing of Hyperspectral Images." *IEEE Transactions on Geoscience and Remote Sensing* 56 (10): 5767. doi:10.1109/TGRS.2018.2825457.

Zhang, G., S. Mei, J. Tian, Y. Feng, and Q. Du. 2019. "Local Sparse Representation Based Spatial Preprocessing for Endmember Extraction." IGARSS 2019 - 2019 IEEE International Geoscience and Remote Sensing Symposium, 278. Yokohama, Japan: IEEE. doi:10.1109/IGARSS.2019.8898577.

Zhang, J., X. Zhang, and L. Jiao. 2021. "Sparse Nonnegative Matrix Factorization for Hyperspectral Unmixing Based on Endmember Independence and Spatial Weighted Abundance." *Remote Sensing* 13 (12): 2348. doi:10.3390/rs13122348.

Zhao, M., J. Chen, and Z. He. 2019. "A Laboratory-Created Dataset with Ground Truth for Hyperspectral Unmixing Evaluation." *IEEE Journal of Selected Topics in Applied Earth Observations and Remote Sensing* 12 (7): 2170. doi:10.1109/JSTARS.2019.2905099.

Zheng, P., Z. Wu, J. Sun, Y. Zhang, Y. Zhu, Y. Shen, J. Yang, Z. Wei, and A. Plaza. 2021. "A Parallel Unmixing-Based Content Retrieval System for Distributed Hyperspectral Imagery Repository on Cloud Computing Platforms." *Remote Sensing* 13 (2): 176. doi:10.3390/rs13020176.

Zhu, Q., L. Wang, W. Zeng, Q. Guan, and Z. Hu. 2021. "A Sparse Topic Relaxion and Group Clustering Model for Hyperspectral Unmixing." *IEEE Journal of Selected Topics in Applied Earth Observations and Remote Sensing* 14: 4014. doi:10.1109/JSTARS.2021.3069574.

Zortea, M. and A. Plaza. 2009. "A Quantitative and Comparative Analysis of Different Implementations of N-FINDR: A Fast Endmember Extraction Algorithm." *IEEE Geoscience and Remote Sensing Letters* 6 (4): 787. doi:10.1109/LGRS.2009.2025520.